

Water-assisted crystallization of amorphous indium zinc oxide films

Alexander Steigert¹, Danny Kojda², Josefa Ibaceta-Jaña³, Daniel Abou-Ras⁴, René Gunder⁴, Nivin Alktash³, Klaus Habicht^{2,5}, Markus R. Wagner⁶, Reiner Klenk⁷, Simone Raoux¹, Bernd Szyszka³, Iver Lauermann⁷ and Ruslan Muydinov^{3,7*}

¹Institute for Nanospectroscopy, Helmholtz-Zentrum Berlin für Materialien und Energie GmbH, Albert-Einstein-Str. 15, 12489 Berlin, Germany

²Department Methods for Characterization of Transport Phenomena in Energy Materials, Helmholtz-Zentrum Berlin für Materialien und Energie GmbH, Hahn-Meitner-Platz 1, 14109 Berlin, Germany

³Chair Technology for Thin Film Devices, Institute of High-Frequency and Semiconductor-system Technologies, Technical University Berlin, Einsteinufer 25, 10587 Berlin, Germany

⁴Department Structure and Dynamics of Energy Materials, Helmholtz-Zentrum Berlin für Materialien und Energie GmbH, Hahn-Meitner-Platz 1, 14109 Berlin, Germany

⁵Institut für Physik und Astronomie, Universität Potsdam, Karl-Liebknecht-Straße 24-25, 14476 Potsdam, Germany

⁶Institute of Solid State Physics, Technische Universität Berlin, Hardenbergstraße 36, 10623 Berlin, Germany

⁷PVcomB, Helmholtz-Zentrum Berlin für Materialien und Energie GmbH, Schwarzschildstraße 3, 12489 Berlin,

Contact: *ruslan.muydinov@tu-berlin.de

Keywords: IZO, thin films, TCOs, crystallisation, water-assisted crystallisation

ABSTRACT

Transparent conductive materials based on indium oxide remain yet irreplaceable in various optoelectronic applications. Amorphous oxides appear especially attractive for technology as they are isotropic, demonstrate relatively high electron mobility and can be processed at low temperatures. Among them is indium zinc oxide (IZO) with a large zinc content that is crucial for keeping the amorphous state but redundant for the doping. In this work we investigated water-free and water containing IZO films obtained by radio frequency sputtering. The correlation between temperature driven changes of the chemical state, the optical and electrical properties as well as the progression of crystallization was in focus. Such characterization methods as: scanning electron microscopy, X-ray diffraction, X-ray photoelectron spectroscopy, Raman spectroscopy, temperature dependent Hall-effect measurements and others were applied. Temperature dependent electrical properties of amorphous IZO and IZO:H₂O films were found to evolve similarly. Based on our experience in In₂O₃:H₂O (In₂O₃:H or IOH) we proposed an explanation for the changes observed. Water admixture was found to decrease crystallization temperature of IZO significantly from ~550°C to ~280°C. Herewith, the presence and concentration of water and/or hydroxyls was found to determine Zn distribution in the film. In particular, Zn enrichment was detected at the film's surface respective to the high water and/or hydroxyl amount. Raman spectra revealed a two-dimensional crystallization of *w*-ZnO which precedes regardless water presence an extensive In₂O₃ crystallization. An abrupt loss of electron mobility as a result of crystallization was attributed to the formation of ZnO interlayer on grain boundaries.

1. Introduction

Indium oxide is a backbone of the mostly used transparent conductive oxides (TCOs). The materials like $\text{In}_2\text{O}_3:\text{Sn}$ (ITO), which is widely used on an industrial scale, and $\text{In}_2\text{O}_3:\text{H}$ (IOH), known for its high electron mobility, are polycrystalline. There are, however, also amorphous semiconducting oxides like $\text{In}_2\text{O}_3:\text{ZnO}$ (IZO), $\text{In}_2\text{O}_3:\text{Ga}_2\text{O}_3$, $\text{In}_2\text{O}_3:\text{Ga}_2\text{O}_3:\text{ZnO}$ (IGZO), $\text{ZnO}-\text{In}_2\text{O}_3-\text{SnO}_2$ and others [1-5]. Besides classical applications as transparent electrodes in various thin film devices, some other curious applications as thermoelectric material [6], photocatalyst [7] and interconnector in fuel cells [8] are also to name. The growing interest in amorphous and nanocrystalline TCOs originates from the isotropy of their properties, lower deposition temperature, and improved stability under mechanical stress, e.g. during bending. It is also worth noticing that the way to transparent electronics faces stability issues [9,10]. Such factors as impurities originating from the processing and composition of amorphous oxides at interface and in the bulk impact the negative-bias temperature stress stability and threshold voltage shift in thin film transistors (TFTs). Annealing of amorphous TCO layers and its conditions represents another crucial factor of influence [11].

Electrical and optical properties of In_2O_3 were summarized and compared for various dopants (Sn-, Zr-, Ti-, H- or unintentional doped (UID)) and crystalline states [12,13]. The experimental correlation between Hall mobility (μ_{Hall}) and density of free electrons (N_e) revealed with some divergence a trend with a plateau in the N_e range of $10^{19}-10^{20} \text{ cm}^{-3}$ common for all In_2O_3 materials. Applying calculations, authors explained this plateau by the ascendant impact of the polar optical phonon scattering (POP) [12]. A linear descending $\mu_{\text{Hall}} = f(N_e)$ correlation at lower N_e was found to point at a prevalence of the ionised impurity scattering (IIS). The position of this dependency along the ordinate axis allows to derive the charge of the ionized impurity. Thus, oxygen vacancies ($\text{V}_{\text{O}}^{\bullet\bullet}$) were proposed to be the major electron donor in UID In_2O_3 [12] whereas in IOH, after T. Koida *et al.* – hydroxyls ($\text{OH}_{\text{O}}^{\bullet}$) [14]. A cooperative doping of In_2O_3 by hydrogen and other metals (M: Ce or W) did not result in a consistent shift of the μ_{Hall} dependency when comparing IOH and IOH:M [15,16]. T. Koida argued that oxygen stoichiometry influenced by $p(\text{H}_2\text{O})$ during deposition may have a predominant impact [16]. Substantial advancement of μ_{Hall} did result however from the water assisted solid phase crystallisation (*spc*), which provides remarkable lateral extension of grains [14,16,17]. Experimental Hall mobility data demonstrate a wide scatter for polycrystalline In_2O_3 samples with $N_e \geq 10^{19} \text{ cm}^{-3}$ which is caused by very different preparation conditions and doping levels [13]. To our knowledge, no systematic correlation between grain size, in particular, lateral grain size and Hall mobility was performed for In_2O_3 films so far. The impact of grain boundaries using an activation energy (*grain boundary barrier heights*) of the temperature dependence of Hall mobility was indirectly estimated [13].

The amorphous state of In_2O_3 films (e.g. IOH, IZO) is a subject of special attention due to the high Hall mobility exceeding $40 \text{ cm}^2/\text{Vs}$, which is comparable to the polycrystalline state. The reason can be different, for instance passivation of dangling bonds by hydrogen in IOH [17,18] or special interconnection of InO_6 octahedra in IZO [19]. J. Robertson attributed enhanced electron mobility in amorphous ionic oxides to the *s*-like conduction bands, attenuating the effects of disorder [20].

Furthermore, one must notice a remarkable thermal stability of the amorphous state in IZO for Zn contents exceeding 16 at. % [21]. In the same work the highest IZO conductivity was detected for 17 at. % Zn. The analysis given by J. E. Medvedeva *et al.* suggested different preferable coordination of In- and Zn-atoms by oxygen to be the reason of stable disorder [22]. Consideration of doping as an origin of *n*-type conductivity in amorphous media is in fact

speculative. However, the first principles based calculations determined $\text{In}_{\text{Zn}}^{\bullet}$ and $\text{V}_{\text{O}}^{\bullet\bullet}$ point defects as the most stable ones in $\text{In}_2\text{O}_3(\text{ZnO})_k$ crystalline solids [23]. A. Walsh calculated that the formation of $\text{V}_{\text{O}}^{\bullet\bullet}$ is energetically favourable along the $\{111\}$ surfaces in In_2O_3 [24]. Thus, he proposed the existence of an interrelated two-dimensional high-mobility electron gas. Our recent study has also revealed the probable impact of metallic indium in under-stoichiometric $\text{In}_2\text{O}_{3-\delta}$ films [17].

A change of optical and electrical properties during crystallization of the initially amorphous IZO films was thoroughly investigated elsewhere [11,21,25]. Obvious degradation of conductivity, especially in an oxygen containing atmosphere, was attributed to crystallization and oxidation of indium to the stoichiometric state. The influence of water presence on IZO crystallization was not studied yet, although it might extend understanding of this material. In this work we analyzed how the sputtered IZO and IZO:H₂O films change during heating. As a function of temperature, we measured their electrical and optical properties and discussed the influence of water.

2. Experiment

The as-deposited IZO films were prepared by radio-frequency (RF, 13.56 MHz) magnetron sputtering from a round \varnothing 3" ceramic IZO (10 wt. % of ZnO) target. Assuming stoichiometric oxygen content we obtain an atomic $[\text{Zn}] / [\text{In}]$ ratio of ~ 0.19 . Square inch Eagle XG (Corning, 0.7 mm thick) glass was used as a substrate. Prior to deposition, substrates were sonicated in organic solvents and washed in a glass-washer using a universal detergent (Mucasol) and de-ionised water. The substrate remained stationary and unheated during deposition. Based on optical and electrical properties, we optimised the target-to-substrate distance and RF-power. Finally, the corresponding values of 40 mm and 60 W were used. The base pressure of the sputtering system was as low as 5×10^{-6} Pa. The inlet of water vapours was varied by an adjustment of the needle valve placed on a pipeline between deposition chamber and water reservoir. Thus adjusted leakage pressure ($p_{\text{leak}}(\text{H}_2\text{O})$) was varied in the range $10^{-3} \dots 10^{-2}$ Pa. Argon with purity grade 5.0 was used as a sputtering gas and a process pressure was fixed at 0.5 Pa. The choice of sputtering conditions was based on our preliminary work on In_2O_3 (see Appendix, Fig. A1).

The as-deposited films were analysed by X-ray photoelectron spectroscopy (XPS) using a standard XPS laboratory module with a non-monochromatic Mg K_{α} X-ray source providing an excitation energy of 1253.6 eV. These analyses were made without breaking vacuum right after depositions in a combined sputter/surface analysis (CISSY) system, described elsewhere [26]. For XPS analysis, ~ 800 nm thick molybdenum films on glass were used as a substrate. The obtained spectra were corrected using an Au standard (using the Au $4f_{7/2}$ emission at a binding energy of 84.0 eV) and fitted in a peak fitting program (PeakFit 4.12). The surface atomic concentrations of elements were calculated from the normalized core level peak area of the elements. The normalization factor was determined considering number of scans, inelastic mean free path (IMFP), ionization cross-section and transmission function. The relativistic IMFP was calculated with QUASES-IMFP-TPP2M software (Ver. 3.0, Quases-Tougaard Inc.©) [27] which uses the TPP-2M formula [28]. Ionization cross-sections were obtained from the Goldberg's tables [29] and the transmission function (T) was calculated from kinetic energy (KE) based on the formula: $T = 840.2335 \times \text{KE}^{-0.9748}$, which was empirically determined from analysis of emission spectra from clean Cu and Au samples [30].

To correlate optical, electrical and microstructural properties, a series of 300 nm thick films was prepared. Each film was annealed at an individual maximum temperature, keeping it there for 30 min. In order to avoid the uncontrolled influence of oxidation during annealing, an N₂ atmosphere with both O₂ and H₂O levels below 1 ppm was used.

X-ray diffraction patterns were acquired using Cu K_α radiation on a D8 Discover diffractometer from Bruker and X'Pert MRD Pro from PANalytical. In both cases 0.02° step size and 1 s step time were used. An α-Al₂O₃ ceramic standard from the National Institute of Standards and Technology (NIST, USA) was used to estimate the crystallite sizes and level of residual stresses in the films. In-situ temperature-dependent XRD experiments were performed in ambient air. The heating speed was 10°C/min; prior to each measurement, the temperature was held for 30 min. Top-view, energy-dispersive X-ray (EDX) analysis was performed on a Jeol JXA-8530F microscope with a silicon-drift detector using 6 kV accelerating voltage, optimized for the 300 nm thick IZO films to reduce the impact of the substrate signal. The analysed area was 50 × 70 μm². Cross-sectional scanning electron microscopy and corresponding EBSD as well as EDX maps were acquired at 15 and 7 kV using a Zeiss UltraPlus scanning electron microscope equipped with a NordlysNano EBSD camera and an XMax80 EDX detector. For this investigation, cross-sectional specimens of the thin films were prepared by mechanical and Ar-ion polishing.

The optical characterisation was performed in the spectral range of 250–2450 nm using a PerkinElmer Lambda 1050 UV–Vis spectrophotometer. Ellipsometry measurements were done on a Sentech Ellipsometer SE 850 with a μ-spot (200 μm spot at the polarizer unit). The incident angle was fixed at 70°, the spectral range was 350 – 850 nm and the value of the refractive index was determined for λ = 632.8 nm. Raman spectroscopy was performed on 300 nm thin films in ambient environment at room temperature (RT) using a high-resolution LabRAM HR800 spectrometer from Horiba with an excitation wavelength of 532 nm. The laser beam was focused using a ×100 / NA=0.9 microscope and excitation power of 0.65 mW. The spectra were recorded using a grating with 600 lines per millimeter and acquisition time of 100 s. We determined the positions of Raman peaks by fitting the experimental data with Lorentzian profiles.

Charge-carrier mobility (μ_e) and charge-carrier density (N_e) of the previously annealed films were determined in ambient air at room temperature by means of resistivity and Hall measurements performed in van der Pauw geometry using an Ecopia HMS-3000 system. Fixed values of the current $I = 5$ mA and magnetic field $B = 0.56$ T were applied. Temperature dependent resistivity and Hall measurements of the as-grown films were performed in a LakeShore HMS-8404 system in argon atmosphere at ambient pressure in the temperature range from room temperature to 600 °C. The mean heating rate was kept at 0.25 K/min. The samples were measured at a maximum current of $I = 3$ mA and maximum magnetic field of $B = 0.9$ T. Current and field were varied to confirm the proportionalities of the Hall voltage.

3. Results and discussion

3.1. Composition, crystallization progress and microstructure

The as-deposited IZO and IZO:H₂O films were analyzed by XPS in order to discover the compositional and chemical differences between them. Main results are presented in Fig. 1 and Fig. A2 (see Appendix). As one can see from Fig. 1a, the presence of water changes both: oxygen stoichiometry and [Zn] / [In] ratio on the surface. Thereby, both: oxygen content and [Zn] / [In] ratio steadily increase with rising $p_{\text{leak}}(\text{H}_2\text{O})$. The O 1s spectra (Fig. A2c) demonstrate the

increasing content of both oxygen fractions: O^{2-} and OH^- when $p_{\text{leak}}(\text{H}_2\text{O})$ rises. Meanwhile, the metal-to-oxygen atomic ratio is expectedly higher ($\sim 1/1$) than the one anticipated for the bulk ($\sim 1/3$). The In 3d XPS spectra show an appreciable shift to lower binding energy when $p_{\text{leak}}(\text{H}_2\text{O})$ increases from 0.002 to 0.02 Pa (Fig. A2a). This contradicts with the known fact that indium has lower electron density in $\text{In}(\text{OH})_3$ as compared to In_2O_3 [31]. Such a mismatch can be explained by the increasing surface concentration of zinc. Indeed, zinc ions, in contrast to In^{3+} , easily form in aqueous solution complexes like $[\text{Zn}(\text{OH})_4]^{2-}$, $[\text{Zn}(\text{H}_2\text{O})_4]^{2+}$ and $[\text{Zn}(\text{H}_2\text{O})_6]^{2+}$. It means that zinc may act as an acceptor of hydroxyls.

At the same time, growing water content causes shifting of the In MNN and Zn LMM Auger maxima to lower kinetic energies (Fig. 1b,c). Considering the In MNN spectrum for In_2O_3 film deposited under knowingly reduced atmosphere (Fig. A1e) and comparing it with the spectra in Fig. 1b one can see that indium is likely in a partially reduced state in the IZO and IZO: H_2O (0.002 Pa) films. This effect is apparently caused by Zn presence. Since its concentration is relatively high and its coordination number is lower than for indium, zinc probably conditions an oxygen lack around indium atoms. This deficiency levels off with growing water content.

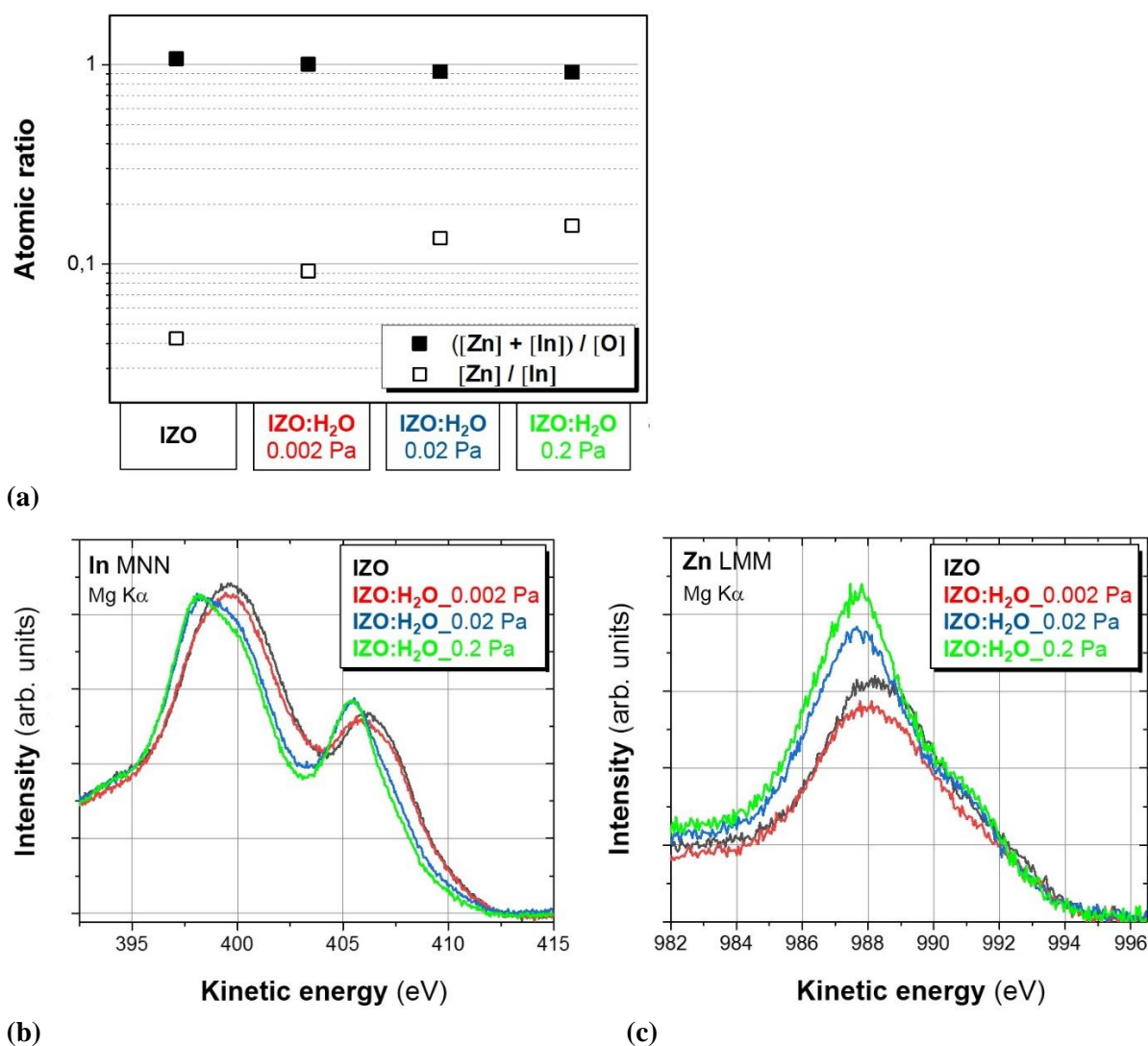


Fig. 1. (a) Atomic ratios based on quantitative analysis of the XPS spectra obtained for In $3d_{5/2}$, Zn $2p_{3/2}$ and O 1s (spectra are shown in Fig. A2) on as-deposited IZO and variously prepared IZO: H_2O films. Auger spectra, leveled to the same baseline in each case: In MNN (b) and Zn LMM (c). The leak water pressure $p_{\text{leak}}(\text{H}_2\text{O})$ used during IZO: H_2O deposition is noticed.

In fact, the In MNN spectrum is rather complex [31] and its detailed analysis goes beyond the scope of current work. Yet, we used the In MNN and In 3d lines to determine the so-called modified Auger parameter a^* , which is calculated by adding the kinetic energy of the Auger peak to the binding energy of the respective photoemission peak. Both Auger and photoemission peaks are affected by charging and band bending effects in the same way, so that a^* is not altered by any of them. It offers a reliable way to identify chemical species. Auger parameters of many compounds have been tabulated, e.g. in [32]. The resulting a^* values for In and Zn are presented in the Table 1. The binding energy (BE) values were taken from the In 3d_{5/2} and Zn 2p_{3/2} peak maxima. The kinetic energy (KE) values were extracted from the In M₅N₄₅N₄₅ (higher intensity contribution) and Zn L₃M₄₅M₄₅ signals of Auger spectra. As shown in figure 1b, the major In MNN Auger peak has in addition to the maximum at ~399.6 eV which appears in all four samples a distinct contribution at KE \approx 398.2 eV being pronounced in the samples with the two highest water contents. This additional peak yields the a^* value equal to ~842.8 eV as opposed to ~844.4 eV resulted from the common maximum. In literature, for In₂O₃ and In(OH)₃ respectively the values ~844.5 eV and ~842.2 eV are given [33]. The values ~2010.1 eV and ~2009.3 eV are correspondingly ascribed to zinc oxide and zinc hydroxylates [34]. In accordance with these values one can deduce if the film's surface is hydrolysed and in which extent (see Table 1). As one can see from the case of lowest water content, ZnO hydrolyzes more readily than In₂O₃.

Summarizing, we suggest that an obvious surface Zn-enrichment in water containing films can be controlled by water adsorption on the films' surface during sputtering.

Table 1. Elucidation of the modified Auger parameter a^* . Possible corresponding compounds are given in the last column. BE values are shown for the In 3d and Zn 2p photoemission lines and KE values for the In MNN and Zn KLL lines.

sample	element	BE (eV)	KE (eV)	a^*	attribution
IZO	In	444.85	399.58	844.43	In₂O₃
	Zn	1021.87	988.20	2010.07	ZnO
IZO:H ₂ O_0.002	In	444.80	399.63	844.43	In₂O₃
	Zn	1021.87	988.00	2009.87	ZnO / Zn(OH)₂
IZO:H ₂ O_0.02	In	444.65	398.17	842.82	In ₂ O ₃ / In(OH)₃
	Zn	1021.82	987.70	2009.52	Zn(OH)₂
IZO:H ₂ O_0.2	In	444.70	398.17	842.87	In ₂ O ₃ / In(OH)₃
	Zn	1021.82	987.75	2009.57	Zn(OH)₂

We excluded from our further consideration the IZO:H₂O film deposited at $p_{\text{leak}}(\text{H}_2\text{O}) = 0.2$ Pa as chemically analogous to the one deposited at $p_{\text{leak}}(\text{H}_2\text{O}) = 0.02$ Pa. The difference between IZO and IZO:H₂O films in crystallization behavior was investigated by a temperature dependent XRD (Fig. 2). Apparently, both water containing films start crystallizing at much lower temperature (~300°C) than the water-free film (~550°C). In all three samples crystallization proceeds briskly: after an abrupt rise, the diffraction maxima intensity remains unchanged upon further heating. This suggests an instant crystallization throughout the entire film thickness. In contrast to the water containing films, the IZO film reveals a pronounced [111]-texture that is in accordance with the lowest surface energy of the {111}-facet [35]. In IZO:H₂O

films we suggest a permanent water enrichment at any forming interface that decreases surface energy. This can explain the absence of a preferable orientation in water containing films.

It is worth to consider how the d_{222} spacing changes with temperature in these films (Fig. 1d). For IZO only a small temperature region is informative, although a linear correlation can be stated. A corresponding value of the thermal expansion coefficient (TEC_{111}) is then $13.7 \times 10^{-6} \text{ K}^{-1}$ which is almost twice as much as the literature value ($7.20 \pm 0.06 \times 10^{-6} \text{ K}^{-1}$) being determined for In_2O_3 powder in a wide temperature range up to $>900^\circ\text{C}$ [36]. Interestingly, this value does not significantly differ from the TEC ($6.2\text{-}6.9 \times 10^{-6} \text{ K}^{-1}$) determined for In_2O_3 at much lower temperatures ($<200^\circ\text{C}$) [37]. For water containing IZO films we can observe changes of the d_{222} in a wider T-range. In both IZO:H₂O samples one may distinguish three regions: a low-T region ($<400^\circ\text{C}$) where the lattice shrinks; a high-T region ($>550^\circ\text{C}$) where the lattice expands; and an intermediate region where the lattice spacing does not reveal a continuous change. The linear thermal expansion detected in IZO:H₂O films is even higher than in IZO. There is also a remarkable difference between films with different water content. The IZO:H₂O with lower water content shows identical lattice constant as the water-free IZO after heating. The IZO:H₂O with more water reveals smaller lattice constant over the whole T-range. This can be explained by the smaller ionic radius of OH^- (1.35 Å) than of O^{2-} (1.38 Å) [38]. Indium hydroxide $\text{In}(\text{OH})_3$ crystallises in a structure type related to bixbyite with the space group $Im\bar{3}$ and $d_{220} = 2.82342 \text{ \AA}$ (PDF 00-058-0465). Thus, the water-rich IZO:H₂O film apparently contains homogeneously distributed OH^- groups which remain even after crystallisation at 600°C .

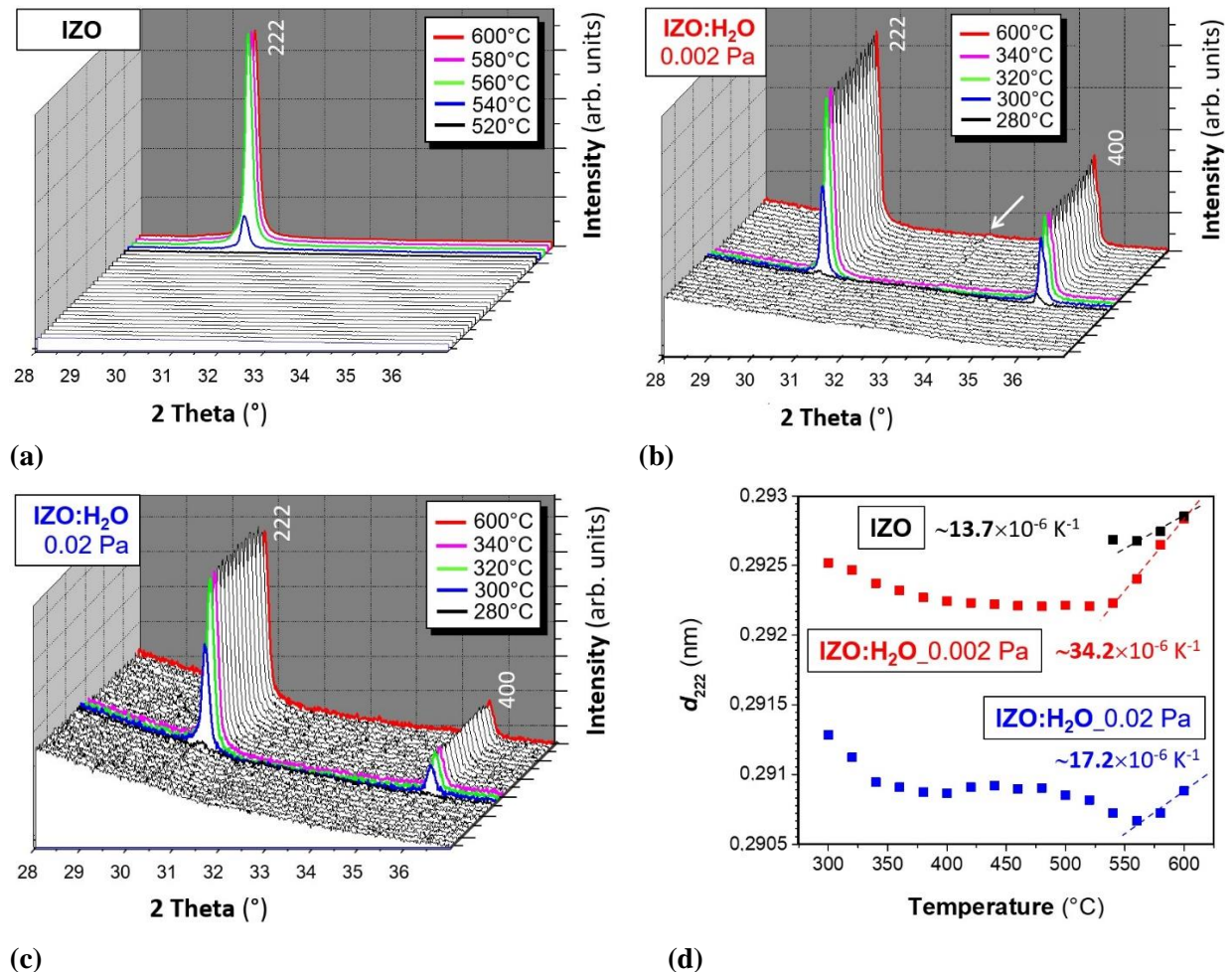
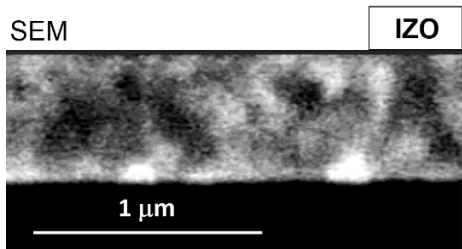


Fig. 2. Temperature-dependent XRD analysis. Patterns were obtained in symmetrical (Bragg-Brentano) scanning mode on 120 nm thick IZO (a) and IZO:H₂O (b,c) films heated in ambient air. The water leak pressure $p_{\text{leak}}(\text{H}_2\text{O})$ used during IZO:H₂O deposition is noticed in labels. The arrow points at the (002)-ZnO diffraction maximum. (d) Calculated change of the d_{222} spacing with temperature for all three films. Longitudinal thermal expansion coefficients (α_{222}) were derived from the high temperature regions of linear dependency.

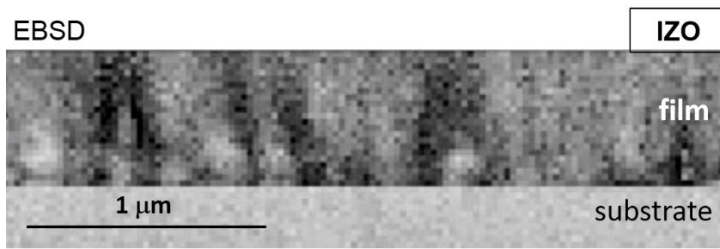
In order to take a closer look at the microstructure of the annealed films, we crystallized thicker (~800 nm, as expected from the deposition time) IZO and IZO:H₂O films at 600°C in air for 1 hour and investigated their polished cross-slices in the electron microscope (see Fig. 2a-f). The SEM images (a, c, and e) represent a channeling contrast which displays different local orientations as different grey values; thus, neighboring grains can be distinguished. In the IZO film (a) individual ≥ 100 nm large grains appear sphere-like, whereas in the IZO:H₂O films (c and e) grains exhibit mostly a columnar pattern, with some volume fraction of smaller, sphere-like grains on the substrate/film interface. A roughly estimated lateral size of columnar grains vary from ~50 nm to ~200 nm. The EBSD pattern-quality maps in Figures 2b, d, and f confirm the differences in microstructure for the IZO and IZO:H₂O films. As visible when comparing the IZO:H₂O films deposited at $p_{\text{leak}}(\text{H}_2\text{O})$ of 0.002 Pa (Fig. 2d) and of 0.02 Pa (Fig. 2f), the volume fraction of the sphere-like grains is much smaller for higher partial H₂O pressures $p_{\text{leak}}(\text{H}_2\text{O})$. This finding can be traced back to the deposition rate, which decreases by about half when $p_{\text{leak}}(\text{H}_2\text{O})$ increases from 0.002 to 0.02 Pa. Apparently the sputtering yield decreases if the H₂O concentration becomes comparable to the concentration of Ar⁺ ions in plasma.

Our in-plane XRD measurements (Fig. A3) disclosed that the lateral grain size in IZO films is generally twice smaller as compared to IZO:H₂O. Comparing heating for 30 min (Fig. A3a) with heating for hours (Fig. A3b) demonstrates that lateral grain size increases with time regardless water presence. No meaningful difference in that sense was found between IZO:H₂O films crystallized at 350°C and 600°C for 30 min. Correlating SEM and in-plane XRD data one may remark that grain growth in IZO:H₂O films proceeds at 600°C most intensively within 1 hour.

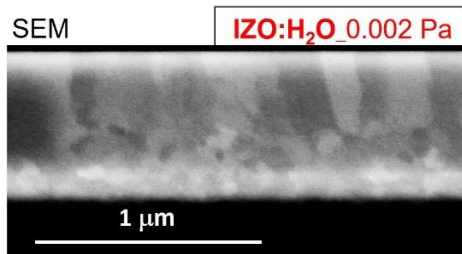
Figures 2g-i show distributions of constituent elements perpendicular to the Si substrates for the three investigated films. In all IZO / IZO:H₂O films, we observe a significant increase of oxygen concentration towards the surface resulting from the annealing in air. At the same time, the concentrations of metals remain homogeneous throughout the IZO thin films. The oxygen signals appear enhanced close to the surface with strong decays towards the volume of the thin films with no or small amounts of water (Fig. 2g,h). In the film containing more water, the oxygen profile linearizes representing faster diffusion (Fig. 2i). Interestingly, the Zn profile probably replicates the oxygen one in the latter case. It allows to suggest further water driven Zn-diffusion towards the surface during annealing. We do not detect any special compositional feature in the region close to the substrate which can explain its different crystallinity. The bulk [In]/[O] and [Zn]/[In] ratios are surprisingly similar for IZO and for the IZO:H₂O with higher water content, whereas the film with smaller water content exhibits remarkably larger [In]/[O] and smaller [Zn]/[In] ratios. As for the [In]/[O] ratio, we suggest that smaller water content might act as a reduction agent in the sputtering plasma, similarly as for the IOH case [17]; however, when at higher $p(\text{H}_2\text{O})$ the sputtering yield decreases, the [In]/[O] ratio becomes smaller again because of water incorporation. The way how the [Zn] changes in the film with $p(\text{H}_2\text{O})$ is not quite clear. An investigation of the RF plasma during sputtering (e.g.) by optical emission spectroscopy may shed light on this aspect.



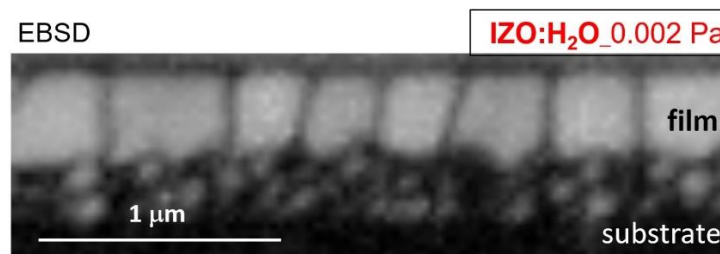
(a)



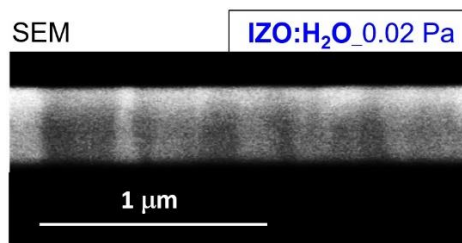
(b)



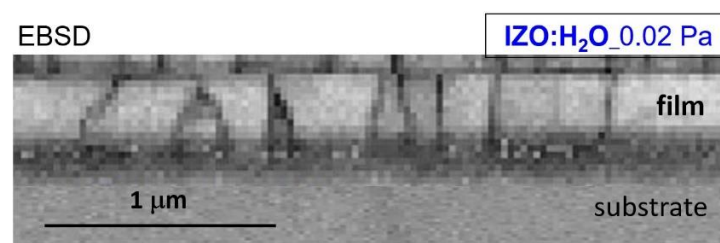
(c)



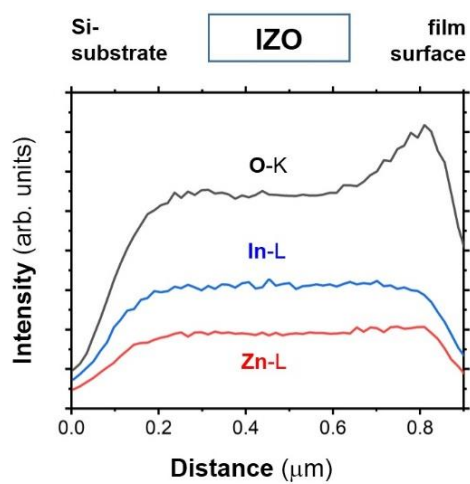
(d)



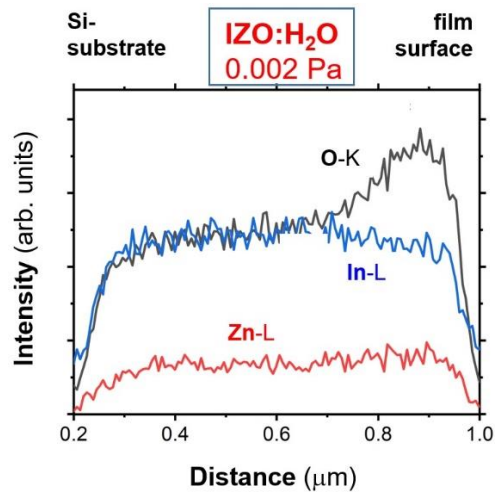
(e)



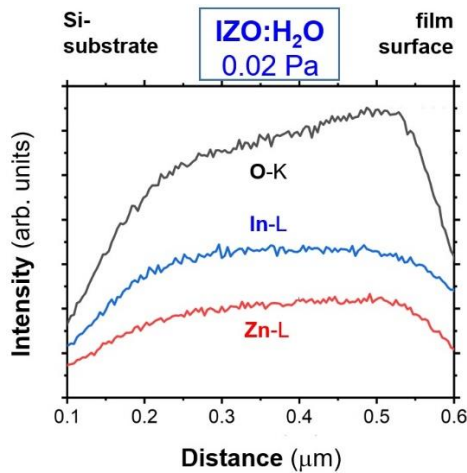
(f)



(g)



(h)



(i)

Fig. 3. Cross-sectional SEM images (a,c,e) and EBSD images (b,d,f) for the IZO and IZO:H₂O films on Si substrates annealed at 600°C for 1 hour in air. (g,h,i) EDX line-scans using the Zn-L, In-L, and O-K X-ray lines. The water leak pressure $p_{\text{leak}}(\text{H}_2\text{O})$ used during IZO:H₂O deposition is noticed in labels.

3.2. Discussion of crystallization behavior

A well-known “amorphization impact” of ZnO in IZO was explained by J. E. Medvedeva with co-workers in terms of very different preferable coordination of In- and Zn-atoms by oxygen [22]. Herewith, the molar ZnO content should be higher than 16% [21] so to provide the interconnection of structural breaking-up sites. The high crystallization temperature of IZO could be then explained by a necessity for active Zn diffusion. To our best knowledge there are no published data on Zn diffusion in amorphous In₂O₃, but we may briefly comment on Zn diffusion in other solids. Thus, in polycrystalline ZnO, active Zn diffusion starts at $T > 1000^\circ\text{C}$ [39], whereas in InP – already at $T > 650^\circ\text{C}$ [40]. Zinc readily forms interstitials and tends to form stable immobile defect clusters [40-42]. In Zn-doped ferrites with the cation sublattice disorder, zinc diffusion is controlled by interstitials at lower $p(\text{O}_2)$ and by vacancies in more oxidative environments [40]. Diffusion via vacancies is rather defined by a structure, whereas diffusion of interstitials strongly depends on size and charge of the cation. In our case we deal with an amorphous In₂O₃ matrix, which is highly disordered in both sublattices. This explains the probable activation of Zn diffusion at lower temperatures than we find for crystalline media in literature. It is known that the transition “crystalline → amorphous”, which is determined in the In₂O₃-ZnO system by the ZnO content, shifts at lower $p(\text{O}_2)$ to a higher ZnO/In₂O₃ ratio [18]. This points at a higher Zn mobility in oxygen deficient In₂O₃.

Our crystallographic data (Fig. 2d) represent isotropic changes of the investigated materials during heating. Instead of just a physical thermal expansion, we detect lattice shrinkage followed by a considerably more intensive expansion than known for polycrystalline In₂O₃. We deal therefore with some chemical, namely compositional changes. It is a matter of fact that oxygen non-stoichiometry in oxides increases with temperature. TEC additionally increases with oxygen desorption due to the following reasons: (i) larger ionic radius of less charged metal ions and (ii) higher repulsion of metal ions at deficiency of negatively charged oxygen ions. A measurable oxygen diffusion in crystalline In₂O₃ films starts at $\sim 600^\circ\text{C}$ [43], whereas IOH reveals oxygen desorption already at $\sim 550^\circ\text{C}$ [14]. The reason why our TEC₁₁₁ values are significantly higher than known for polycrystalline In₂O₃ can arise from more active oxygen desorption from our

films with smaller crystallites. It was reported that the annealing of crystalline IZO in argon resulted in an increase of the lattice constant by $\sim 0.02 \text{ \AA}$ for the ZnO-rich region and by $\sim 0.04 \text{ \AA}$ for the ZnO-poorer region [21]. Such an influence of the Zn admixture displays either its inertia to oxygen release or even some inhibition of this process. This is generally consistent with our data showing the highest TEC value for the film with the lowest Zn-content.

The influence of water presence in the film can be considered as follows. When larger O^{2-} is displaced by smaller OH^- , then the lattice must shrink, however the overall oxidation state of In is simultaneously forced to decrease, that increases the ionic radius of In^{n+} ($n < 3$). Comparing IZO:H₂O films with lower and higher water content, we realise that the former has both: less OH^- and a higher $[\text{In}]/[\text{O}]$ ratio than the latter (Fig. 3) that comprehensively explains the corresponding difference in d_{222} values over the entire considered temperature region.

The IZO:H₂O films reveal general compression at heating from 300°C to 550°C (Fig. 2d). This trend is more pronounced in the film with higher Zn and water contents. Discussing accompanying compositional changes, we must consider probable release of water and desorption of In^0 and Zn^0 at low $p(\text{O}_2)$. It is known that $\text{In}(\text{OH})_3$ dissociates in inert atmosphere at temperatures above 200°C [44], however decomposition starts already with its melting at $\sim 150^\circ\text{C}$. Similarly, $\text{Zn}(\text{OH})_2$ starts decomposing after its melting at $\sim 125^\circ\text{C}$. Indium desorbs from IOH already at $T > 160^\circ\text{C}$ [14,17]. In our work on IOH we identified metallic indium in the films and proposed its reaction with hydroxyls with hydrogen release [17]. At higher temperature, zinc desorption becomes also probable as it starts desorbing from ZnO:Al at $T > 300^\circ\text{C}$ [45]. The following processes: (i) desorption of water; (ii) desorption of an indium excess; (iii) oxidation of metallic indium by water / hydroxyl may explain the lattice shrinkage as a result of simultaneous indium oxidation and Zn-enrichment. Here we take into account that the ionic radius of Zn^{2+} (0.60 Å for the coordination number IV, 0.68 Å (V) and 0.74 Å (VI)) is generally smaller than the same of In^{3+} (0.62 Å (IV) and 0.80 Å (VI)) [38]. Interestingly, M. P. Taylor *et al.* have found combining XRD and TEM, that the d_{222} spacing decreases from $\sim 2.9 \text{ \AA}$ to 2.77 \AA when IZO transforms from a crystalline to an amorphous state via embedding of ZnO [21]. This suggests the space effect of smaller Zn^{2+} ions to prevail over the incidental reduction of In^{+3} found by XPS spectroscopy in our amorphous IZO films. Therefore exactly the larger Zn-concentration in water-rich IZO:H₂O is responsible for a more pronounced lattice shrinkage at 300-350°C. We speculate that Zn desorption starts at $\sim 400^\circ\text{C}$ after which the trend reverses.

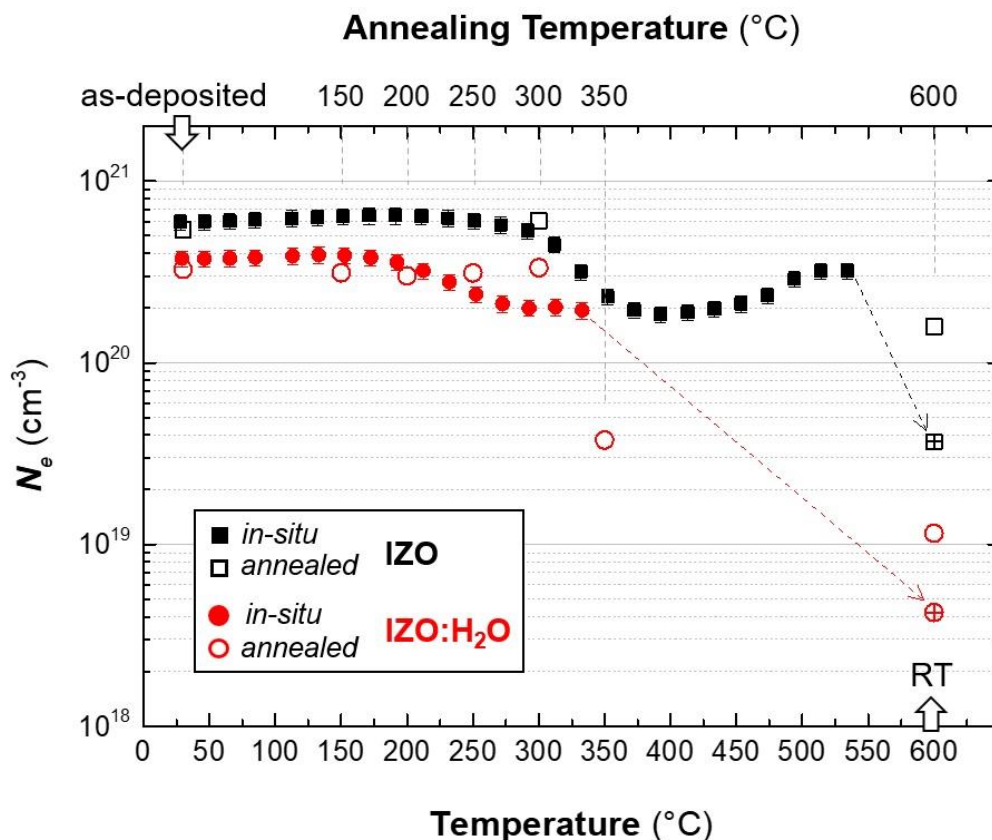
Comparing all three films annealed at 600°C, one finds that IZO and water-poor IZO:H₂O reveal despite initially different Zn-content the same lattice spacing whereas the water-rich IZO:H₂O film contains probably captured hydroxyls.

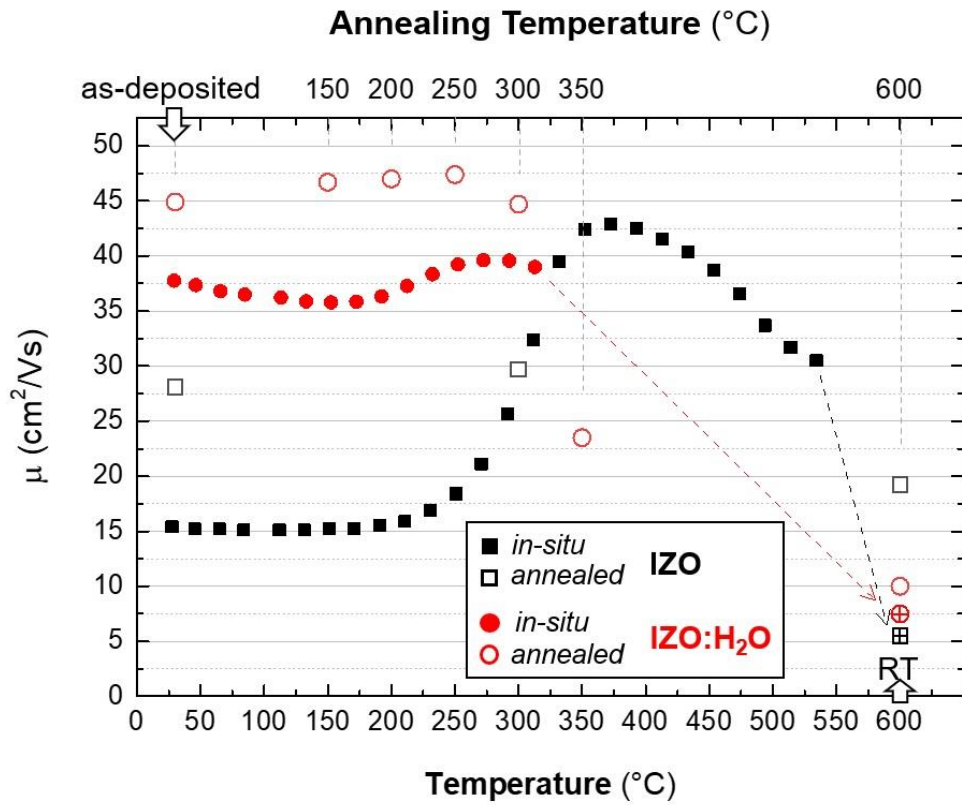
3.3. Electrical properties of amorphous IZO and IZO:H₂O

For the investigation of electrical properties we considered only IZO and IZO:H₂O with the lowest water content because the water-rich IZO:H₂O films demonstrated in the as-deposited state about two orders of magnitude higher sheet resistance and remained even after annealing at 600°C in a partially hydrolyzed state. We measured their electrical properties during annealing in an inert atmosphere to avoid an oxidation. The *in-situ* measurements on single 120 nm thick IZO and IZO:H₂O films were compared with the room temperature measurements performed on individual 300 nm thick films annealed at different temperatures (Fig. 4). Thinner films were

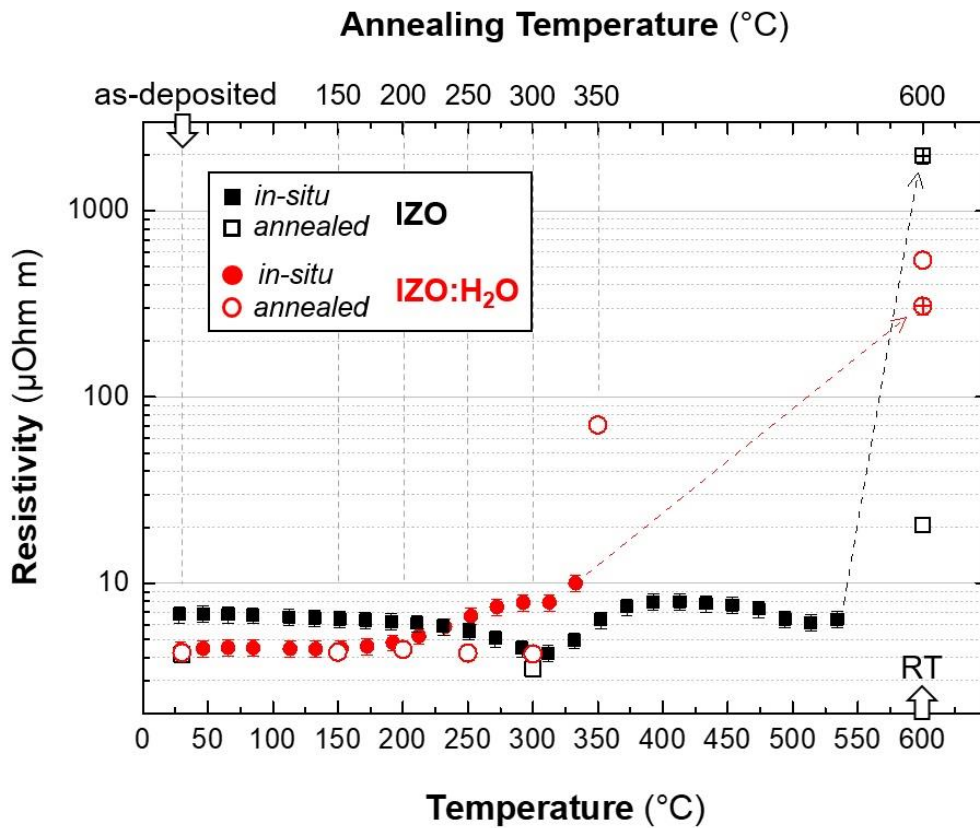
taken in order to maximize the Hall-signal, whereas consideration of thicker films was necessary for the optical investigations (see A.4).

The *in-situ* Hall-measurements revealed different electrical behavior of the IZO and IZO:H₂O films. One may, however, find similar regions in N_e (Fig. 4a) and μ_e (Fig. 4b) temperature dependencies, in which the presence of water shifts the extrema to lower temperatures. Three regions can be distinguished before crystallization. In the low temperature region, N_e and μ_e remain almost unchanged. At a certain temperature N_e starts decreasing and μ_e starts increasing in both films. Herewith, in IZO:H₂O both parameters start changing at 160-180°C almost simultaneously, resulting in a rising resistivity (Fig. 4c). In IZO, μ_e significantly increases starting from ~230°C, while N_e starts decreasing from ~280°C. This situation results in a changing trend of resistivity, which decreases in the region 230...310°C and increases above ~310°C till ~380°C. In the third temperature range the concentration of free electrons remains almost unchanged in IZO:H₂O and slightly increases in the IZO case. At the same time, the Hall-mobility drops in IZO:H₂O film insignificantly, whereas in IZO we detect a considerable reduction of μ_e . A massive fall of conductivity at $T > 333^\circ\text{C}$ and $> 534^\circ\text{C}$ was detected for the IZO:H₂O and IZO films respectively and the measurements were interrupted. This phenomenon accords with the beginning of crystallisation in both cases (see Fig. 2). After heating up to 600°C and cooling down to room temperature the Hall effect and resistivity measurements were also performed on these samples in the same assembly (Fig. 4).





(b)



(c)

Fig. 4. Results of the temperature dependent *in-situ* Hall measurements performed in inert atmosphere for the 120 nm thick IZO and IZO:H₂O films on glass (close symbols). Crossed symbols represent values obtained on these films after *in-situ* measurements and cooling down to RT. For comparison, the electrical

properties measured at RT for the annealed at corresponding temperatures 300 nm thick films are shown (open symbols).

So to untangle the intrinsic structural and chemical changes of IZO and IZO:H₂O during heating and understand the results of in-situ Hall measurements better, the corresponding 300 nm thick films were annealed at different temperatures and investigated at RT. For IZO:H₂O more individual samples were annealed corresponding to more temperature points so to investigate early crystallization stages by Raman spectroscopy [46,47]. According to this analysis (see Appendix, Fig. A4), In₂O₃ crystallization starts with formation of the crystalline (In-O) / (Zn-O) interface, which appears as a specific ZnO mode at 600°C in IZO and at 300°C in IZO:H₂O films. The appearance of this interface diminishes in IZO:H₂O at higher annealing temperatures, while the modes of crystalline ZnO emerge from 350°C. These effects point at a ZnO phase separation. Herewith, a compressive strain can be admitted in ZnO that agrees with the intensive In₂O₃ grain growth (Fig. 3c). In the IZO film annealed at 600°C, both: bulk and interface ZnO-modes are active. It fits with an isotropic microcrystallinity observed (see Fig. 3a). At the same time, the ZnO phase reveals a large concentration of electronic defects, which may result from some doping. Finally, one can deduce that the ZnO phase separation precedes the In₂O₃ crystallization in both IZO and IZO:H₂O materials. The XRD evidence of a ZnO phase formation in IZO at T ≥ 500°C was also reported in literature [11].

As seen from Fig. 4a, the N_e values and trends generally coincide for differently measured samples of both compositions, however thicker films reveal higher N_e after annealing at 600°C (open *versus* crossed points). Additionally, thick IZO:H₂O does not demonstrate any N_e drop at T > 180°C, which was characteristic for the thinner film. A similar effect was observed by B. Yaglioglu *et al.* after annealing of 100 nm thick IZO films in air at 200°C when N_e dropped for the most part within 40 min [48]. As our *in-situ* measurements were not performed in a flow of inert gas, oxygen presence cannot be excluded.

The values of the Hall mobility obtained during heating do not agree well with the values measured at RT for both compositions. Thus, thicker films reveal considerably higher μ_e values at T < 300°C. This suggests some structural or compositional difference between thicker and thinner as-deposited films regardless water presence. However, the difference is more pronounced in the IZO case. The impact of IZO thickness on μ_e change with temperature was also stressed in literature [21]. The small value (15 cm²/Vs) as we obtained for the thinner as-deposited amorphous IZO film is, however, untypical for this material [11,25,49-51]. According to J. E. Medvedeva and D. B. Buchholz, a high electron mobility (50-60 cm²/Vs) in amorphous IZO is explained by formation of chains from corner-shared InO₆ polyhedra [19,22]. Herewith, deposition temperature was found to play a crucial role. In case of the pulsed laser deposition (PLD) a leap of μ_e occurs when the deposition temperature rises from -50°C up to -25°C [22]. Considering our films at higher temperatures, the $\mu_e = f(T)$ trends match up with some offset for IZO:H₂O films, but not for pure IZO.

Resistivity values agree well for IZO:H₂O films at T ≤ 200°C. At further heating, ρ of the thicker film increases steeper than that of the thinner film, demonstrating some temperature delay. Finally, the IZO:H₂O films crystallized at 600°C show meaningful differences only in N_e but not in μ_e , and a comparable resistivity in spite of very different lateral sizes of crystallites (see Fig. A3).

As we pointed out above, initial (as-deposited) states of the thick and thin IZO films differed in terms of electrical properties. At 300°C, however, N_e , μ_e and ρ values become very

similar for those films, which might point at similar states of these materials. After crystallisation, the thinner and longer annealed IZO film revealed a two orders of magnitude higher resistivity than we measured for the thicker one. This difference is caused by a significantly stronger decline of both μ_e and N_e during crystallization of the thin IZO film. We notice that the 300 nm thick crystalline IZO film has grains of much smaller lateral size than the 120 nm thick IZO one (see Fig. A3). This means that grain boundaries in the thin IZO film represent much larger energy barriers for free electrons than in the thick film.

Apart from discussion of electrical properties given right below we present in Appendix (A.5) some relevant information on energy levels in amorphous IZO from literature.

3.4. Discussion of electrical properties of amorphous IZO

A remarkable thermal stability of the amorphous state in IZO, electrical and optical properties of this material, and a change of the phase composition with heating were thoroughly studied elsewhere [11,21,25,49-51]. This TCO belongs to those with relatively high electron mobility. The reason why a disorder in amorphous oxides does not enhance scattering of electrons is appropriately explained by J. Robertson [20]. As pointed out above, the main factor for high electron mobility in amorphous IZO is the formation of certain structural chains. Another amorphous material with the same μ_e level is the as-deposited IOH [14,17]. In this case a passivation of dangling bonds by hydrogen ions was proposed to support high electron mobility [17,18]. Indeed, despite rather ionic character (~60%) of chemical bonds in In_2O_3 , one may expect a formation of hydrogen bonds in IOH.

Polycrystalline In_2O_3 based TCOs, such as $\text{In}_2\text{O}_3\text{:Zr}$ and $\text{In}_2\text{O}_3\text{:Mo}$ films reveal even higher electron mobility, which exceeds $80 \text{ cm}^2/\text{Vs}$ [52-54]. In the latter case, a shared hybridization of Mo 4d and In 5s states at the bottom of the conduction band was suggested to provide unusually low IIS in this material [55]. Even higher electron mobility exceeding $100 \text{ cm}^2/\text{Vs}$ is known for crystalline IOH films with grains of a submicron lateral size [14,16,17]. Water- or hydrogen-free crystalline In_2O_3 materials demonstrate μ_e values even beyond $150 \text{ cm}^2/\text{Vs}$ but for much lower N_e levels than in IOH [12]. A critical influence of the scattering on grain-boundaries in polycrystalline In_2O_3 -based conductors was observed and discussed in the literature [13]. However, a vast majority of the reported XRD data represent information on transversal crystallinity of In_2O_3 films that is not compatible with the measured lateral conductivity. We see that the reason for high electron mobility can be very different in various In_2O_3 based oxides.

In general, the conductivity of oxides is influenced by $p(\text{O}_2)$, temperature and presence of admixtures [21,25,49,50,56]. The n -type conductivity in IZO can be provided by $\text{V}_\text{O}^{\bullet\bullet}$ and $\text{Zn}_\text{i}^{\bullet\bullet}$ point defects [56]. Ionic radii of In^{3+} (IV) and Zn^{2+} (IV) are quite close (see above) and the existence of $\text{In}_{\text{Zn}}^\bullet$ defects cannot be excluded. In fact, In-doped ZnO is known and characterized, but it does not represent a very good conductor [57,58]. In a turn, Zn_{In}' defects are the electron acceptors and if present, would suppress n -type conductivity. However, a contribution of such point defects to conductivity is restricted by a strong distortion of the structural 6-fold oxygen coordination [59]. Considering IZO:H₂O we have to take into account additional point defects due to the presence of water. In the well-known, high-mobility crystalline IOH material, T. Koida *et al.* suggested the $(\text{OH})_\text{O}^\bullet$ defects to be responsible for the n -type conductivity [14]. We also detected metallic indium in IOH films and identified that it can energetically be a source of additional free electrons in In_2O_3 [17]. Moreover, the *in-situ* investigation of the In / In_2O_3 interface with respect to its electric properties and electron energy levels discovered the

formation of a 2D electron gas, which acts as a surface donor in sufficiently thin indium films [60]. Summarizing numerous data on In_2O_3 based TCOs, one can state that the factors which determine the N_e level the most are oxygen stoichiometry and temperature. Our as-deposited water-free IZO films revealed smaller $[\text{In}]/[\text{O}]$ ratio compared to the water-poor IZO: H_2O films (Fig. 3g,h). It means that the higher initial N_e level in former case cannot be explained by oxygen stoichiometry.

A presence of Zn^{2+} may influence the concentration of free electrons in IZO also as follows. Metallic zinc and indium form a kind of galvanic pair with a potential difference of ~ 0.32 V in neutral aqueous environment [61,62]. This means that In (III) reduces more readily than Zn (II) in a face of oxygen deficiency. We speculate that exactly this factor provides somewhat higher N_e in as-deposited IZO due to higher Zn-concentration.

It is known that the film's surface is being heated by RF-plasma during deposition. Practically, this resulted in crystallization of our IOH films starting from ~ 150 nm thickness due to the lack of water [17]. We expect a similar effect of water depletion in the upper region of our thick IZO: H_2O films, which, however, does not lead to crystallization because of zinc presence. This circumstance may explain why N_e behaves in the thick IZO: H_2O and IZO films similarly, i.e. remains almost unchanged below 300°C (Fig. 4a). Conversely, N_e starts decreasing at $T > 180^\circ\text{C}$ in the thin IZO: H_2O film. The latter can result from the oxidation of indium by water, which activates above the melting point of metallic indium. Metallic indium can form in IZO films as well, since RF-plasma provides a significant impact of UV irradiation, facilitating disproportionation of indium in sub-stoichiometric oxides [63]. According to the same figure, oxidation by external oxygen demands higher temperatures and is suggested to start at $T > 300^\circ\text{C}$. In fact, the thick IZO film underwent the same heat influence of plasma. This impact stipulates higher initial μ_e values found for thicker films of both compositions (Fig. 4b).

The following drop of mobility at $T > 275^\circ\text{C}$ in IZO: H_2O and at $T > 345^\circ\text{C}$ in IZO has probably different reasons. In the former case, the earliest crystallization stage (see Fig. 2b and Fig. A3b), in which a network of the $\text{In}_2\text{O}_3 / \text{ZnO}$ interfaces forms, coincides with a lowering of electron mobility. In IZO film Hall mobility drops more dramatic and it seems to interrelate with the N_e increase. At this temperature, thermodynamic stability already matters. Thus, ZnO is less stable than In_2O_3 , referring to their free Gibbs energies of formation, which are respectively $-(379.8 \pm 0.5)$ [64] and $-(661.3 \pm 4.2)$ $\text{kJ}\cdot\text{mol}^{-1}$ [65] at 400°C . Furthermore, ZnO demonstrates at low $p(\text{O}_2)$ an anomalously high dissociation rate as compared to the thermodynamically predicted one [66]. This means that Zn-O bonds are less stable than In-O bonds that may result in a formation of zinc interstitials providing additional free electrons.

A massive decrease of conductivity after crystallization has most probably same reasons in all cases. In case of the *in-situ* measurements, a part of the N_e decrease originated from the temperature difference, because the crystallized samples were measured at RT. Another part of the same, resulted from the oxidation of indium which was stronger in thin films because of possible oxygen presence in the chamber amplified by longer temperature treatment. Based on Raman spectroscopy, we assume a formation of the ZnO-rich grain-boundaries disturbing lateral conductivity in both materials. In IZO films, however, the bulk $[\text{Zn}]$ concentration was found to be significantly larger than in IZO: H_2O films. The Hall mobility was found to markedly differ exactly for thin and thick crystalline IZO films. Since the thinner IZO film demonstrated a much larger lateral size of crystallites and a much lower μ_e value, than the thicker one, we suggest a significantly higher Zn-enrichment of grain-boundaries in the former case.

4. Conclusions

In this work we compared the RF-sputtered, water free IZO films with those containing water. The chemical impact of water in conjunction with the temperature driven change of conductivity was discussed. Being heated water containing and water free IZO films in amorphous state revealed similar changes of N_e and μ_e but with some temperature offsets. An increasing oxidation state of indium is responsible for the N_e decline whereas ZnO dissociation is suggested to provide additional free electrons. Water may become an active internal oxidizing agent above the melting point of metallic indium. The oxidation of indium by oxygen gas traces apparently needs higher temperature exceeding 250°C. Water driven Zn-depletion in as-deposited films and water release during heating stipulated a much lower crystallization temperature of IZO:H₂O as compared to IZO. Crystallization in both cases was found to start with the formation of the Raman active In₂O₃-ZnO interface that leads to the ZnO segregation at the grain boundaries. This was suggested to be responsible for an abrupt loss of electron mobility in crystalline IZO films of both kinds. IZO films crystallized in sphere like grains of < 200 nm size whereas IZO:H₂O revealed a columnar microstructure with 2-3 times larger grains. A change of the d_{222} lattice spacing with temperature up to 600°C was compared for these materials. It was found that water might remain in initially water-rich IZO:H₂O films even after crystallization at 600°C.

5. Acknowledgements

We sincerely thank Mr. Jörg Nissen from the Zentraleinrichtung Elektronenmikroskopie (ZELMI) at TU Berlin for the planar EDX analyses. This work was also supported by the Scholarship Becas Chile-DAAD 2017/91645541 and the German Federal Ministry for Economic Affairs and Energy (BMWi) under contract number 0324095H (speedCIGS).

6. References

- [1] H. Yabuta, M. Sano, K. Abe, T. Aiba, T. Den, H. Kumomi, K. Nomura, T. Kamiya, H. Hosono, High-mobility thin-film transistor with amorphous InGaZnO₄ channel fabricated by room temperature rf-magnetron sputtering, *Appl. Phys. Lett.* 89 (2006) 112123.
- [2] J. H. K. Jeong, H. W. Yang, J. S. Park, Y.G.Y.G. Mo, H. D. Kim, High performance thin film transistors with cosputtered amorphous indium gallium zinc oxide channel, *Appl. Phys. Lett.* 91 (2007) 113505.
- [3] C. A. Hoel, T. O. Mason, J. F. Gaillard, K. R. Poepelmeier, Transparent conducting oxides in the ZnO-In₂O₃-SnO₂ system. *Chem. Mater.* 22 (2010) 3569–3579.
- [4] T. Kamiya, K. Nomura, H. Hosono, Present status of amorphous In-Ga-Zn-O thin-film transistors. *Sci. Technol. Adv. Mater.* 11 (2010) 044305.
- [5] K. Nomura, H. Ohta, A. Takagi, T. Kamiya, M. Hirano, H. Hosono, Room-temperature fabrication of transparent flexible thin-film transistors using amorphous oxide semiconductors. *Nature* 432 (2004) 488-492.
- [6] G. Korotcenkov, V. Brinzari, and M.-H. Ham, In₂O₃-Based Thermoelectric Materials: The State of the Art and the Role of Surface State in the Improvement of the Efficiency of Thermoelectric Conversion, *Crystals* 8 (2018) 14-51.
- [7] Z. Li, P. Zhang, T. Shao, J. Wang, L. Jin, X. Li, Different nanostructured In₂O₃ for photocatalytic decomposition of perfluorooctanoic acid (PFOA), *Journal of Hazardous Materials* 260 (2013) 40– 46.
- [8] L. V. Morozova, M. V. Kalinina, P. A. Tikhonov, I. A. Drozdova, and O. A. Shilova, Synthesis and Study of Solid Solutions Based on Indium Oxide in the In₂O₃-ZrO₂ (HfO₂) Systems as a Material for Fuel Cell Interconnectors, *Inorganic Materials: Applied Research* 7/5, Springer, 2016, pp. 658–663. ISSN 2075-1133.

- [9] H.-R. Lee and J.-G. Park, High-Stability Transparent Amorphous Oxide TFT with a Silicon-doped Back-channel Layer, *Journal of the Korean Physical Society*, 65/7 (2014) 1174-1178.
- [10] Y.-S. Shiah, K. Sim, Y. Shi, K. Abe, S. Ueda, M. Sasase, J. Kim and H. Hosono, Mobility–stability trade-off in oxide thin-film transistors, *Nature Electronics*, 4 (2021) 800–807.
- [11] P. Barquinha, G. Gonçalves, L. Pereira, R. Martins, E. Fortunato, Effect of annealing temperature on the properties of IZO films and IZO based transparent TFTs, *Thin Solid Films* 515 (2007) 8450–8454.
- [12] N. Preissler, O. Bierwagen, A. T. Ramu, J. S. Speck, Electrical transport, electrothermal transport, and effective electron mass in single-crystalline In_2O_3 films. *Phys. Rev. B* 88 (2013) 085305.
- [13] M. V. Frischbier, H. F. Wardenga, M. Weidner, O. Bierwagen, J. Jia, Y. Shigesato, A. Klein, Influence of dopant species and concentration on grain boundary scattering in degenerately doped In_2O_3 thin films, *Thin Solid Films* 614 (2016) 62–68.
- [14] T. Koida, M. Kondo, K. Tsutsumi, A. Sakaguchi, M. Suzuki, and H. Fujiwara, Hydrogen-doped In_2O_3 transparent conducting oxide films prepared by solid-phase crystallization method, *J. Appl. Phys.* 107 (2010) 033514.
- [15] E. Kobayashi, Y. Watabe, T. Yamamoto, and Y. Yamada, Cerium oxide and hydrogen co-doped indium oxide films for high efficiency silicon heterojunction solar cells, *Sol. Energy Mater. Sol. Cells* 149 (2016) 75–80.
- [16] T. Koida, Y. Ueno, and H. Shibata, 2018. In_2O_3 -Based Transparent Conducting Oxide Films with High Electron Mobility Fabricated at Low Process Temperatures *Phys. Status Solidi A* 215 (2918) 1700506.
- [17] R. Muydinov, A. Steigert, M. Wollgarten, P. P. Michałowski, U. Bloeck, A. Pflug, D. Erfurt, R. Klenk, S. Körner, I. Lauermann, and B. Szyszka, Crystallisation phenomena of In_2O_3 :H films, *Materials* 12 (2019) 266. doi:10.3390/ma12020266
- [18] H. F. Wardenga, M. V. Frischbier, M. Morales-Masis, A. Klein, In Situ Hall Effect Monitoring of Vacuum Annealing of In_2O_3 :H Thin Films. *Materials* 8 (2015) 561–574.
- [19] D. B. Buchholz, Q. Ma, D. Alducin, A. Ponce, M. Jose-Yacamán, R. Khanal, R., J. E. Medvedeva, and R. P. H. Chang, The Structure and Properties of Amorphous Indium Oxide *Chem. Mater.* 26 (2014) 5401–5411.
- [20] J. Robertson, Physics of amorphous conducting oxides, *Journal of Non-Crystalline Solids* 354 (2008) 2791–2795.
- [21] M. P. Taylor, D. W. Readey, M. F. A. M. van Hest, C. W. Teplin, J. L. Alleman, M. S. Dabney, L. M. Gedvilas, B. M. Keyes, B. To, J. D. Perkins, and D. S. Ginley, The Remarkable Thermal Stability of Amorphous In-Zn-O Transparent Conductors, *Adv. Funct. Mater.* 18 (2008) 3169–3178.
- [22] J. E. Medvedeva, D. B. Buchholz, and R. P. H. Chang, Recent Advances in Understanding the Structure and Properties of Amorphous Oxide Semiconductors, *Adv. Electron. Mater.* 3 (2017) 1700082.
- [23] H. Peng, J.-H. Song, E. M. Hopper, Q. Zhu, T. O. Mason, and A. J. Freeman, Possible n-type carrier sources in $\text{In}_2\text{O}_3(\text{ZnO})_k$, *Chem. Mater.* 24 (2012) 106–114. dx.doi.org/10.1021/cm202020g
- [24] A. Walsh, Surface oxygen vacancy origin of electron accumulation in indium oxide, *Appl. Phys. Lett.* 98 (2011) 261910.
- [25] B. Yaglioglu, H.-Y. Yeom, and D. C. Paine, Crystallization of amorphous In_2O_3 –10 wt % ZnO thin films annealed in air, *Appl. Phys. Lett.* 86 (2005) 261908.
- [26] I. Lauermann, A. Steigert, CISSY: A station for preparation and surface/ interface analysis of thin film materials and devices. *J. Large-Scale Res. Fac.* 2 (2016) A67.
- [27] QUASES Software packages to characterize surface nano-structures by analysis of electron spectra. <http://www.quases.com/products/quases-imfp-tpp2m/> (accessed on Jul 31, 2020)
- [28] H. Shinotsuka, S. Tanuma, C. J. Powell, & D. R. Penn, Calculations of electron inelastic mean free paths. X. Data for 41 elemental solids over the 50 eV to 200 keV range with the relativistic full Penn algorithm, *Surface and Interface Analysis* 47/9 (2015) 871-888.
- [29] S. M. Goldberg, C. S. Fadley, S. Kono, Photo-ionization cross-sections for atomic orbitals with random and fixed spatial orientation, *J. Electron Spectrosc. Relat. Phenom.* 21/4 (1981) 285-363.
- [30] R. Tschöke, Untersuchung der Phasenbildung in Cu/In-Legierungen als Ausgangsmaterialien für CuInS_2 -Dünnschichtsolarzellen. Diploma thesis, Fachbereich Physik der Freien Universität Berlin, 2010.

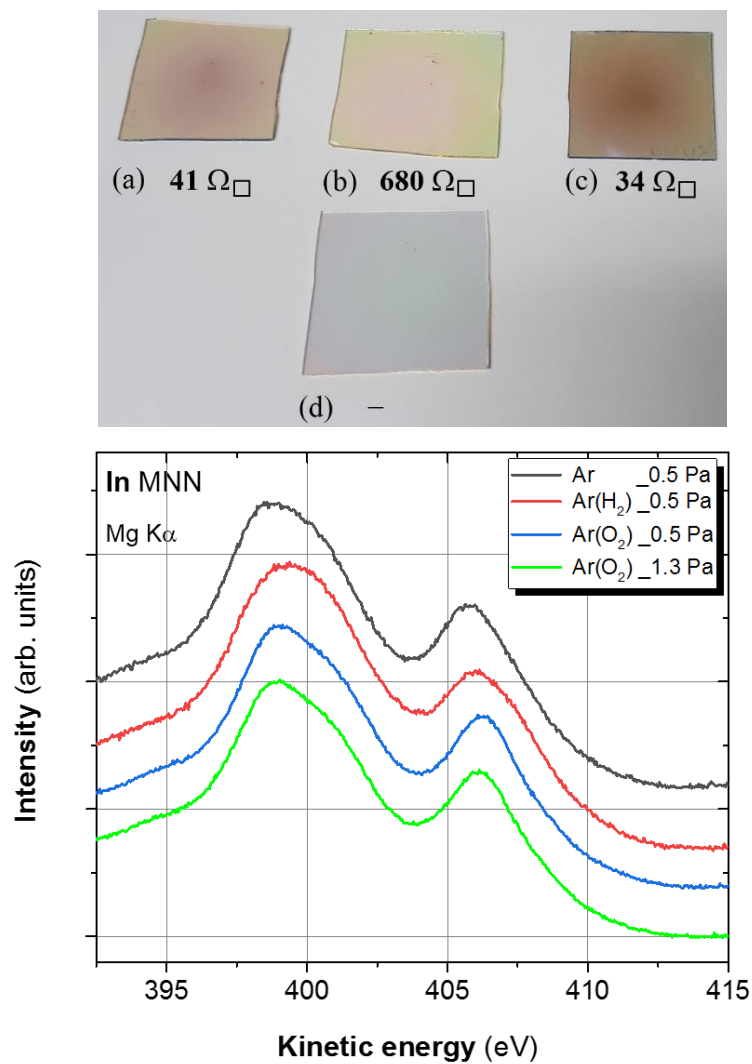
- [31] Z. M. Detweiler, S. M. Wulfsberg, M. G. Frith, A. B. Bocarsly, S. L. Bernasek, The oxidation and surface speciation of indium and indium oxides exposed to atmospheric oxidants, *Surface Science* 648 (2016) 188–195.
- [32] J. Chastain (Ed.), *Handbook of X-ray photoelectron spectroscopy*, Perkin-Elmer Corp. USA, 1992, 261 p. ISBN 0-9627026-2-5.
- [33] I. Majumdar, V. Parvan, D. Greiner, R. Schlatmann, I. Lauer mann, Effect of Na from soda-lime glass substrate and as post-deposition on Cu(In,Ga)Se₂ absorbers: A photoelectron spectroscopy study in ultra-high vacuum, *Appl. Surf. Sci.* 538 (2021) 148085. <https://doi.org/10.1016/j.apsusc.2020.145941>
- [34] E. Rauwel, A. Galeckas, P. Rauwel, M. F. Sunding, and H. Fjellvag, Precursor-Dependent Blue-Green Photoluminescence Emission of ZnO Nanoparticles, *J. Phys. Chem. C* 115 (2011) 25227–25233.
- [35] A. Walsh, and C. Richard, A. Catlow, Structure, stability and work functions of the low index surfaces of pure indium oxide and Sn-doped indium oxide (ITO) from density functional theory, *J. Mater. Chem.* 20 (2010) 10438-10444.
- [36] K. D. Kundra and S. Z. Ali, Thermal expansion of In₂O₃, *J. Appl. Cryst.* 3/6 (1970) 543-545.
- [37] S. B. Qadri, C. Fahed, H. Kim, A. Pique', N. A. Mahadik, and M. V. Rao, Thermal expansion studies of indium-iron oxide, *Phys. Status Solidi B* 248/4 (2011) 928–930.
- [38] R. D. Shannon, Revised Effective Ionic Radii and Systematic Studies of Interatomic Distances in Halides and Chalcogenides, *Acta Cryst.* A32 (1976) 751-767.
- [39] M. A. Neves Nogueira, W. B. Ferraz, A. C. Soares Sabioni, Diffusion of the ⁶⁵Zn Radiotracer in ZnO Polycrystalline Ceramics, *Materials Research* 6/2 (2003) 167-171.
- [40] B. Tuck, and A. Hooper, Diffusion profiles of zinc in indium phosphide, *J. Phys. D: Appl. Phys.* 8 (1975) 1806-1821.
- [41] M. A. Gluba, N. H. Nickel, and N. Karpensky, Interstitial zinc clusters in zinc oxide, *Phys. Rev. B* 88 (2003) 245201.
- [42] J.-H. Lee, M. Martin, H.-I. Yoo, Self- and impurity cation diffusion in manganese-zinc-ferrite, Mn_{1-x-y}Zn_xFe_{2+y}O₄, *J. Phys. Chem. Solids* 61/10 (2000) 1597-1605.
- [43] G. P. Wirtz, H. P. Takiar, Oxygen Diffusion in Vapor-Deposited Indium Oxide Films. *J. Am. Ceram. Soc.* 64/12 (1981) 748–752.
- [44] N. Koga, T. Kimizu, Thermal Decomposition of Indium (III) Hydroxide Prepared by the Microwave-Assisted Hydrothermal Method, *J. Am. Ceram. Soc.* 91 (2008) 4052–4058.
- [45] T. Koida, T. Kaneko, and H. Shibata, Carrier Compensation Induced by Thermal Annealing in Al-Doped ZnO Films, *Materials* 10/2 (2017) 141. doi:10.3390/ma10020141
- [46] V. H. Castrejón-Sánchez, E. Camps, M. Camacho-López, Quantification of phase content in TiO₂ thin films by Raman spectroscopy, *Superf. Vacío* 27/3 (2014) 88-92.
- [47] O. M. Berengue, A. D. Rodrigues, C. J. Dalmaschio, A. J. C. Lanfredi, E. R. Leite, and A. J. Chiquito, Structural characterization of indium oxide nanostructures: a Raman analysis, *Journal of Physics D: Appl. Phys.* 43/4 (2010) 045401.
- [48] B. Yaglioglu, Y.-J. Huang, H.-Y. Yeom, D.-C. Paine, A study of amorphous and crystalline phases in In₂O₃–10 wt.% ZnO thin films deposited by DC magnetron sputtering, *Thin Solid Films* 496 (2006) 89 – 94.
- [49] K. Yamada, B. Shinozaki, K. Yano, and H. Nakamura, The temperature dependence of Hall mobility of the oxide thin film In₂O₃-ZnO, *Journal of Physics: Conference Series* 400 (2012) 042069.
- [50] T. Ashida, A. Miyamura, Y. Sato, T. Yagi, N. Taketoshi, T. Baba, Y. Shigesato, Effect of electrical properties on thermal diffusivity of amorphous indium zinc oxide films, *J. Vac. Sci. Technol.* A25 (2007) 1178-1183.
- [51] S. Kim, D. Kim, J. Byeon, J. Lim, J. Song, S. Park, C. Park, and P. Song, Transparent amorphous oxide semiconductor as excellent thermoelectric materials, *Coatings* 8/12 (2018) 462.
- [52] M. Morales-Masis, E. Esteban Rucavado, R. Monnard, L. Barraud, J. Holovský, M. Despeisse, M. Boccard, C. Ballif, Highly Conductive and Broadband Transparent Zr-Doped In₂O₃ as Front Electrode for Solar Cells, in *IEEE Journal of Photovoltaics* 8/5 (2018) 1202-1207. doi: 10.1109/JPHOTOV.2018.2851306
- [53] C. Warm Singh, Y. Yoshida, and D. W. Readey, C. W. Teplin, J. D. Perkins, P. A. Parilla, L. M. Gedvilas, B. M. Keyes, and D. S. Ginley, High-mobility transparent conducting Mo-doped In₂O₃ thin films by pulsed laser deposition, *J. Appl. Phys.* 95/7 (2004) 3831-3833.

- [54] S. Parthiban, K. Ramamurthi, E. Elangovan, R. Martins, E. Fortunato, R. Ganesan, High-mobility molybdenum doped indium oxide thin films prepared by spray pyrolysis technique, *Materials Letters* 62 (2008) 3217–3219.
- [55] D. S. Bhachu, D. O. Scanlon, G. Sankar, T. D. Veal, R. G. Egdell, G. Cibin, A. J. Dent, C. E. Knapp, C. J. Carmalt, and I. P. Parkin, Origin of high mobility in molybdenum-doped Indium oxide, *Chem. Mater.* 27 (2015) 2788–2796. doi: 10.1021/cm503896h
- [56] D. S. Ginley, H. Hosono, D. C. Paine (Eds.), *Handbook of Transparent Conductors*, Springer, Boston, MA, 2011. doi 10.1007/978-1-4419-1638-9
- [57] A. Hafdallah, F. Yanineb, M. S. Aida, N. Attaf, In doped ZnO thin films, *Journal of Alloys and Compounds* 509 (2011) 7267–7270.
- [58] T.-H. Fang, S.-H. Kang, Optical and physical characteristics of In-doped ZnO nanorods, *Current Applied Physics* 10/4 (2010) 1076-1086.
- [59] Y.-B. Lu, T. L. Yang, Z. C. Ling, W.-Y. Cong, P. Zhang, Y. H. Li and Y. Q. Xin, How does the multiple constituent affect the carrier generation and charge transport in multicomponent TCOs of In-Zn-Sn Oxide, *J. Mater. Chem. C*, 3 (2015) 7727-7737.
- [60] M. Nazarzahdemoafi, F. Titze, S. Machulik, C. Janowitz, Z. Galazka, R. Manzke, M. Mulazzi, Comparative study of the electronic structures of the In and Sn/In₂O₃ (111) interfaces, *Phys. Rev. B* 93 (2016) 081303.
- [61] P. Vanýsek, *Handbook of Chemistry and Physics*, 81th ed., Electrochemical Series; CRC Press LLC: Boca Raton, FL, USA, 2000. ISBN 978-0849304811.
- [62] A. J. Bard, R. Parsons, and J. Jordan, *Standard Potentials in Aqueous Solutions*, Marcel Dekker, New York, 1985. ISBN 0-8247-7291-1.
- [63] B. Clafin, H. Fritzsche, The Role of Oxygen Diffusion in Photoinduced Changes of the Electronic and Optical Properties in Amorphous Indium Oxide, *J. Electron. Mater.* 25 (1996) 1772–1777.
- [64] J. D. Cox, D. D. Wagman, V. A. Medvedev, *CODATA Key Values for Thermodynamics*, Hemisphere Publishing Corp., New York, 1984.
- [65] T. J. Kallarackel, Gibbs free energies of formation of indium (III) oxide and sulphate, *Mineral Processing and Extractive Metallurgy IMM Transactions section C* 87 (1978) C165-C169.
- [66] E. A. Secco, Decomposition of zinc oxide, *Can. J. Chem.* 38 (1960) 596-601.

APPENDIX

A.1. In_2O_3 films

It is known that sputtering of TCOs requires optimization of the oxygen content in a gas mixture. Taking into account the spectrum shape in case of the oxidized In-state which also corresponds to the most resistive In_2O_3 film, one can find quite the same spectrum shape in case of the film sputtered just in argon (Fig. A1). This film revealed however best combination of high transparency and high conductivity, therefore we used for our experiments on IZO films the same sputtering conditions as in the case (a).



(e)

Fig. A1. Crystalline 300 nm thick In_2O_3 films sputtered at 60 W RF-power in various gas-mixtures: (a) Ar; (b,d) Ar / 1 vol.% O_2 , (c) Ar / 5 vol.% H_2 . Films (a,b,c) were deposited at $p_{\text{tot}} = 0.5$ Pa and film (d) at 1.3 Pa in the same deposition system as the IZO films. Sheet resistance is shown for the first three conductive samples. (e) Auger spectra for the analogous films obtained on Mo/glass substrates.

A.2. XPS data

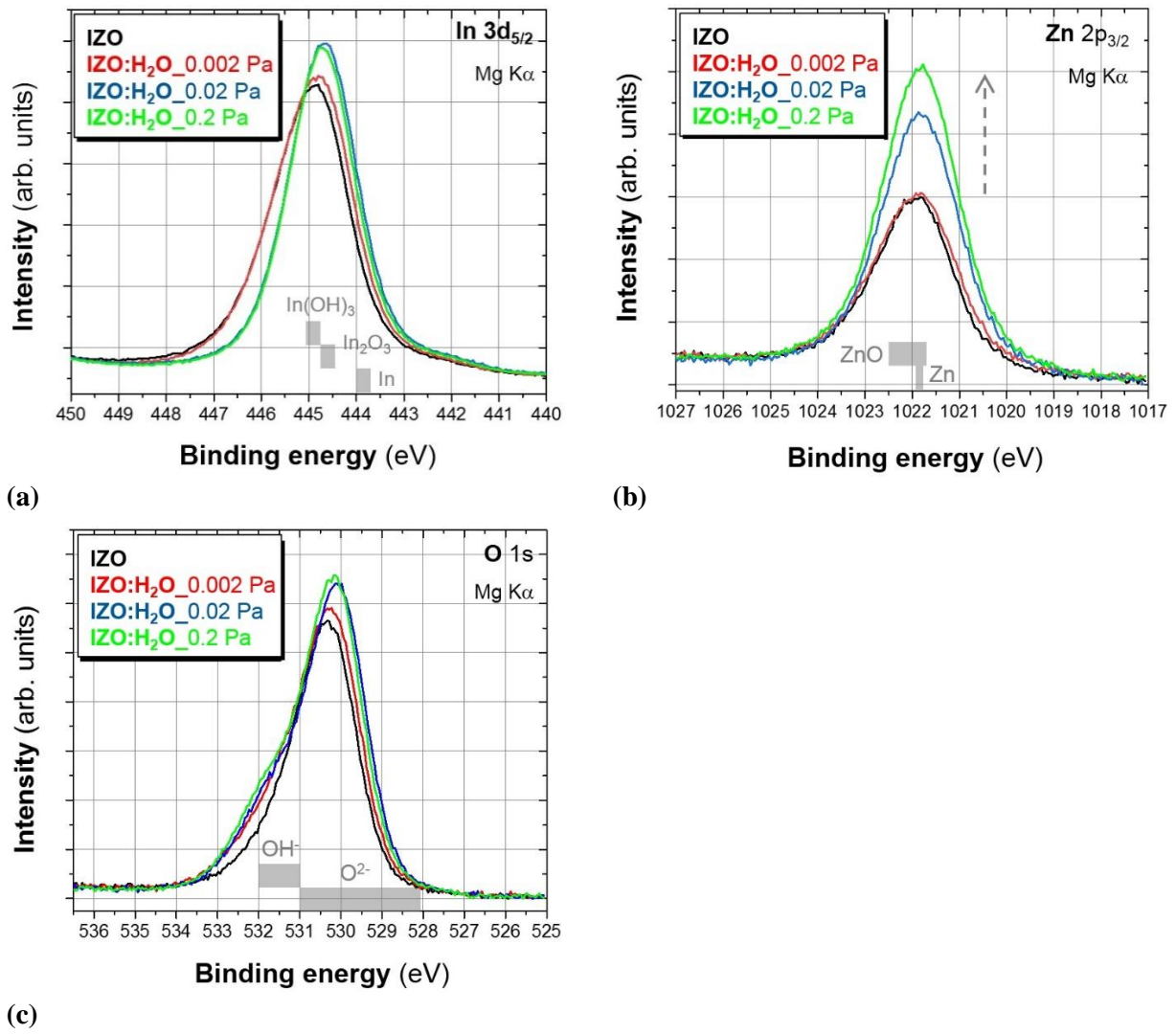
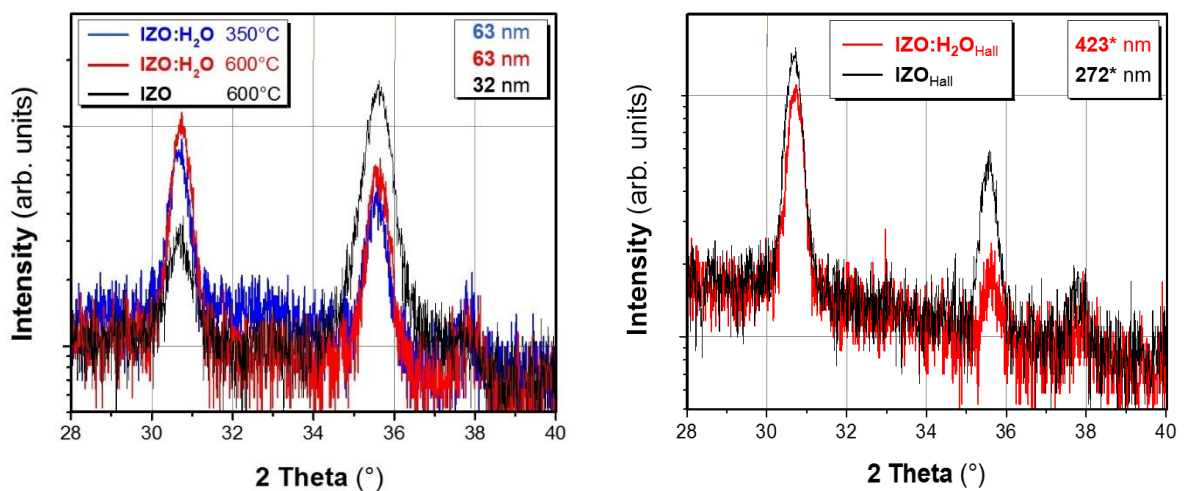


Fig. A2. XPS spectra for In 3d_{5/2} (a), Zn 2p_{3/2} (b) and O 1s (c) obtained on variously prepared as-deposited IZO and IZO:H₂O films on Mo/glass substrate. Spectra were aligned to the same background level. Energy regions corresponding to the different chemical states of elements [1] are shown by grey squares. The leak pressure $p_{\text{leak}}(\text{H}_2\text{O})$ used during IZO:H₂O deposition is noticed.

A.3. In-plane XRD data



(a) (b)

Fig. A3. XRD patterns obtained in an in-plane scanning mode for the 300 nm films crystallized at given temperatures in 30 min (a) and for the 120 nm thick films crystallized during *in-situ* Hall measurements (b). In the right inset the lateral areas of coherent scattering determined using Scherrer formula are given. Starlets denote a formal character of the corresponding values, because the X-ray optics used could not provide reliable determination of areas of coherent scattering larger than ~250 nm.

A.4. Correlation between optical and electrical properties

Table A1. Electrical, optical and microstructural properties of the differently prepared 300 nm thick IZO and IZO:H₂O films on glass. Fitting of the optical data was performed using the RIG-VM software developed at Fraunhofer IST [2]. Using Drude term for free electrons and the effective mass $m^* = 0.3 m_e$ taken for In₂O₃ from the literature [3], the $N_{e \text{ opt}}$ and $\mu_{e \text{ opt}}$ have been determined. Refractive indices (n) were determined by ellipsometry.

		as-depo	150°C	200°C	250°C	300°C	350°C	600°C
IZO	E_g (eV)	3.27				3.35		3.44
	$N_{e \text{ opt}}$ (cm ⁻³)	4.24·10²⁰				4.92·10²⁰		2.12·10²⁰
	$\mu_{e \text{ opt}}$ (cm ² /Vs)	36.1				36.5		16.7
	ρ_{opt} (Ω·cm)	4.08·10 ⁻⁴				3.48·10 ⁻⁴		1.77·10 ⁻³
	$N_{e \text{ Hall}}$ (cm ⁻³)	5.39·10²⁰				6.03·10²⁰		1.58·10²⁰
	$\mu_{e \text{ Hall}}$ (cm ² /Vs)	28.1				29.7		19.2
	ρ (Ω·cm)	4.12·10 ⁻⁴				3.49·10 ⁻⁴		2.06·10 ⁻³
	n	1.97				1.94		2.03
IZO:H ₂ O	E_g (eV)	3.27				3.31	3.38	3.44
	$N_{e \text{ opt}}$ (cm ⁻³)	2.94·10²⁰	2.93·10²⁰	2.77·10²⁰	2.81·10²⁰	3.16·10²⁰	7.78·10¹⁹	1.51·10²⁰
	$\mu_{e \text{ opt}}$ (cm ² /Vs)	49.0	50.1	52.2	53.2	44.2	12.4	39.7
	ρ_{opt} (Ω·cm)	4.34·10 ⁻⁴	4.25·10 ⁻⁴	4.31·10 ⁻⁴	4.18·10 ⁻⁴	4.47·10 ⁻⁴	6.48·10 ⁻³	1.04·10 ⁻³
	$N_{e \text{ Hall}}$ (cm ⁻³)	3.27·10²⁰	3.13·10²⁰	3.01·10²⁰	3.12·10²⁰	3.34·10²⁰	3.75·10¹⁹	1.15·10¹⁹
	$\mu_{e \text{ Hall}}$ (cm ² /Vs)	44.9	46.7	47.0	47.4	44.7	23.5	10
	ρ (Ω·cm)	4.25·10 ⁻⁴	4.28·10 ⁻⁴	4.42·10 ⁻⁴	4.22·10 ⁻⁴	4.19·10 ⁻⁴	7.07·10 ⁻³	5.86·10 ⁻²
	n	2.00	2.01	2.01	2.00	2.09	2.10	2.05

Electrical and optical properties of the separately annealed 300 nm thick films are summarized in the Table A1. As one can see, optical band-gap is not affected by the presence of water, however crystallization leads to an increase of the band gap energy E_g . We observed similar effect in the IOH material that was explained by a downward shift of the upper valence level available for the optical transition as a result of crystallization [4]. Large area (50 × 70 μm) planar EDX analysis gave for the IZO films in question the [Zn] / [In] atomic percent ratio around ~0.2, that is slightly smaller than that in the target. This ratio increased by ~0.05 from room temperature to 300°C and decreased by ~0.1 from 300°C to 600°C. In IZO:H₂O films the [Zn] / [In] ratio was found to be smaller than in IZO ones by ~0.02 over the whole temperature region considered. This compositional arrangement between crystallized IZO and IZO:H₂O

matches with the data of cross-sectional EDX analysis (compare Fig. 2d and Fig. 2e). The ellipsometric data, described by the Drude-Lorentz model [5], deliver generally higher refractive indices for the IZO:H₂O films than for the IZO ones. Accepting the interrelation between refractive index and density of a solid, one can find that IZO:H₂O material reaches its maximum density at about 350°C ($n_D \approx 2.10$) whereas IZO – at 600°C ($n_D \approx 2.03$). In literature, $n_D \approx 2.093$ was reported for the crystalline undoped In₂O₃ [6].

Considering the concentration of free electrons and their mobility, one can find a principal difference between IZO and IZO:H₂O films crystallized at 600°C (Table 1). In the former case optical and electrical data agree as if IZO would remain isotropic after crystallization. Herewith, the ρ_{opt} is only ~15% lesser than the ρ_{Hall} . Cross-sectional SEM images demonstrate in this case homogeneously distributed small (< 100 nm) sphere-like crystallites that corresponds to a quasi-isotropic allocation of grain boundaries (Fig. 3a). In case of the crystalline IZO:H₂O material, both optical charge carrier's concentration and, especially, optical mobility are larger than electrically derived values. Thus, the resulting ρ_{opt} is ~60 times smaller than the ρ_{Hall} . It points at a significant inter-grain scattering which is not reflected by the optical measurements. According to the SEM data (Fig. 3c,e), crystalline IZO:H₂O films reveal columnar microstructure where grain boundaries are arranged mostly perpendicular to the surface and the longitudinal size of crystallites approaches film thickness. This explains why the lateral electrical resistivity is much larger than the longitudinal optical one in this case.

Within the isotropic X-ray amorphous state of both materials the electrically and optically determined N_e and μ_e values reveal coinciding dependency on temperature. The absolute magnitudes differ however in a way: $N_{e\ opt} < N_{e\ Hall}$ and $\mu_{e\ opt} > \mu_{e\ Hall}$. Such a difference between optical and electrical properties may result from the different behaviour of electrons in a constant electric field (Hall measurements) *versus* high frequency electric field of light. Thereby, resistivity determined by both methods matches up well. In case of crystalline ZnO:Al it would point at a negligible impact of the IIS [2], however in amorphous In₂O₃ this kind of scattering was found to prevail over scattering due to the structural disorder [7].

A.5. Energy levels in amorphous IZO

So to understand if any practical use of IZO:H₂O films can be proposed, we give here some information on how energy levels of VBM (valence band maximum) and CBM (conduction band minimum) change in IZO materials. J. Kim *et al.* reported these data for several amorphous oxide semiconductors including IZO with different [Zn] / [In] ratios [8]. Spectroscopic measurements shown that both VBM and CBM energies get shallower when Zn content increases. At the same time fundamental E_g increases as well. The covalent bonding of Zn 3d-orbitals with the O 2p-orbitals is attributed to the E_{VBM} decrease. According to the first principle calculations, conduction band in In₂O₃ is comprised of the antibonding state yielded by the strong In 5s–O 2p interactions whereas hybridization of the In 5s / Zn 4s orbitals influences the E_{CBM} in IZO [9].

According to J.-W. Jeon *et al.* the optical band gap and N_e decrease in amorphous IZO as a result of heating in oxygen containing atmosphere up to 300°C [10]. It disagrees with our data obtained for IZO annealed in dry N₂ (Table A1). It shows that oxygen lack in amorphous IZO causes doping-like effect even at temperatures below 300°C.

A.6. Raman spectroscopy data

Below we discuss the Raman spectra shown in Fig. A4. For comparison, we describe the spectra of the In_2O_3 and ZnO films first. In the former case we detect peaks at 127, 303, 360 and 491 cm^{-1} , which correspond to the crystalline modes of cubic bixbyite structure E_{2g} , E_{1g} , E_{2g} and A_{1g} respectively [11-13]. ZnO film shows peaks at 275, 514, 583 and 644 cm^{-1} . The peak at 583 cm^{-1} corresponds to the E_1 mode of crystalline wurtzite phase [14]. Meanwhile, other peaks represent the modes of defective lattice with lower symmetry [15]. Apparently, our sputtered ZnO film is very defect-rich since the measured Raman spectrum noticeably differs from the one which is known for single crystalline ZnO [16].

The as-deposited IZO film reveals broad Raman peaks without specific features of the individual crystalline bixbyite In_2O_3 or wurtzite ZnO phase. Such behavior is typical for amorphous materials where atomic disorder produces broad distribution of the states with close vibrational energies. Other investigations of amorphous IZO samples by resonant Raman spectroscopy have not revealed characteristic peaks either [17-19]. The annealing at 300°C does not result in any remarkable change of the Raman spectrum. After annealing at 600°C, the IZO film reveals peaks related to the specific *b*- In_2O_3 vibrational phonon modes at 127, 303 and 360 cm^{-1} . One can also ascribe the broad peak at 419 cm^{-1} to a conflation of the *w*-ZnO vibrational modes at 407 cm^{-1} (E_1) and 437 cm^{-1} (E_2). The pronounced hump in the range from 500 to 650 cm^{-1} was also found in other studies on IZO and described as overlapping of the modes A_1 (583 cm^{-1}) from *w*-ZnO and E_{2g} (629 cm^{-1}) from *b*- In_2O_3 [17]. Such an overlay was suggested to represent predominant vibration of wurtzite sublattice on the (In-O) / (Zn-O) interfaces. Another ZnO related mode is detected at 333 cm^{-1} that relates to the multiphonon processes which occur when the phonon wave vectors considerably remove from the centre of the Brillouin zone. This phenomenon represents some imposed defectiveness. For instance, the two-phonon bands, which are often detected in such materials as graphene, silicon and transition metals, contain valuable information about the phonon dispersion, the electron-phonon and electron-photon couplings, doping, and strain [20-22]. In conclusion, the Raman spectrum of the X-ray crystalline IZO film is dominated by the modes of highly defective *w*-ZnO phase and shows fairly weak modes of *b*- In_2O_3 structure. This fingerprint does not quite coincide with the corresponding XRD pattern where expressly crystalline *b*- In_2O_3 phase but no *w*-ZnO was detected (Fig. 2a). We speculate that Raman effect is less pronounced in textured fine crystalline In_2O_3 .

Analogously to the IOH we expected early crystallization stages in IZO:H₂O aroused by water desorption. Hence the number of low annealing temperatures was intentionally increased in contrast to the IZO case. Raman spectra of the as-deposited and annealed at $T < 300^\circ\text{C}$ films do not show characteristic Raman peaks. The IZO:H₂O film annealed at 300°C present similar broad hump as an evidence of vibration on the (In-O) / (Zn-O) interface as in the case of crystalline IZO. This overlaid mode weakens with annealing temperature that may point at ZnO agglomeration. Crystallization of IZO:H₂O at 350°C correlates with an occurrence of the *b*- In_2O_3 specific Raman peaks at 127 and 303 cm^{-1} . These modes become more pronounced in the film annealed at 600°C, in which the 360 cm^{-1} mode comes also up. Additionally, the weak peaks at 591 cm^{-1} and 627 cm^{-1} emerge, which we attribute to the modes E_1 at 583 cm^{-1} (*w*-ZnO) and E_{2g} at 629 cm^{-1} (*b*- In_2O_3). A blue shift in *w*-ZnO case can be explained by the impact of compressive strain.

Interestingly, the characteristic Raman modes of *w*-ZnO do not stand out in the X-ray crystalline IZO:H₂O films. That contradicts with the XRD data where ZnO phase was detected exactly in the IZO:H₂O film rather than in IZO (Fig. 2a,b). The following factors can explain it: (i) water driven ZnO agglomeration on the surface during long-term XRD experiment; and (ii) probable dissociation of ZnO with Zn release in case of annealing for Raman measurements at $T \geq 400^\circ\text{C}$ and low $p(\text{O}_2)$ environment in a glovebox.

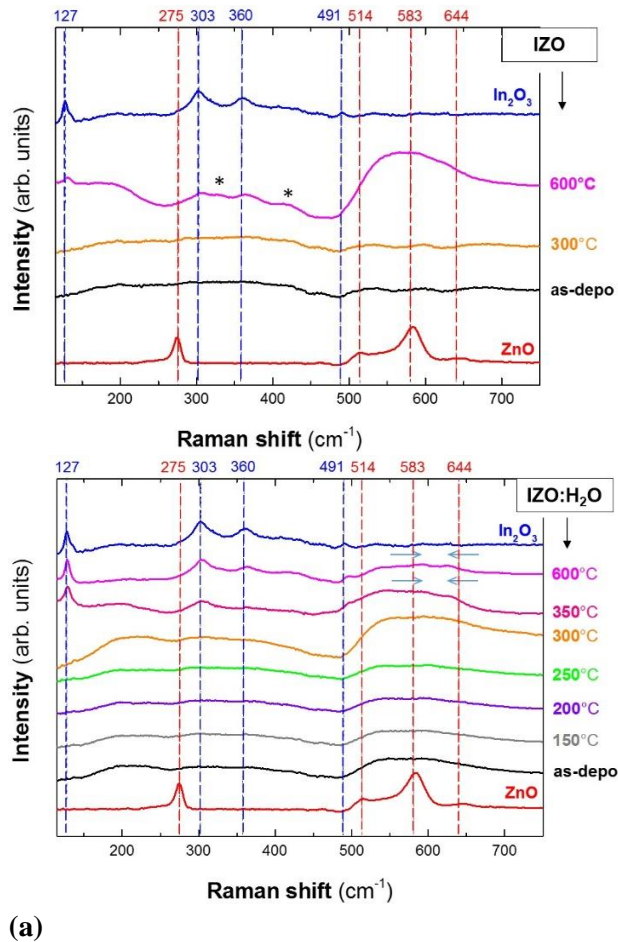


Fig. A4. Raman spectra for the 300 nm thick IZO (a) and IZO:H₂O (b) films on glass. In all cases the spectrum of the substrate was subtracted. Different annealing temperatures are compared, and each curve belongs to an individual sample. Annealing was performed in a dry N₂ atmosphere under pressure of 1.03 bar. Additionally, Raman spectra for the individual RF-sputtered X-ray crystalline In₂O₃ (blue) and ZnO (red) films are presented. Specific known Raman modes are indicated by the dotted lines colored respectively [11-15]. Starlet symbols and green arrows indicate the modes which need additional comments given in the text.

REFERENCES

- [1] J. Chastain (Ed.), Handbook of X-ray photoelectron spectroscopy, Perkin-Elmer Corp. USA, 1992, 261 p. ISBN 0-9627026-2-5.
- [2] A. Pflug, V. Sittinger, F. Ruske, B. Szyszka, G. Dittmar, Optical characterization of aluminum-doped zinc oxide films by advanced dispersion theories, Thin Solid Films 455–456 (2004) 201–206.
- [3] N. Preissler, O. Bierwagen, A. T. Ramu, J. S. Speck., Electrical transport, electrothermal transport, and effective electron mass in single-crystalline In₂O₃ films. Phys. Rev. B 88 (2013) 085305.

- [4] R. Muydinov, A. Steigert, M. Wollgarten, P. P. Michałowski, U. Bloeck, A. Pflug, D. Erfurt, R. Klenk, S. Körner, I. Lauermaun, and B. Szyszka, Crystallisation phenomena of $\text{In}_2\text{O}_3\text{:H}$ films, *Materials* 12 (2009) 266.
- [5] S. D'Elia, N. Scaramuzza, F. Ciuchi, C. Versace, G. Strangi, R. Bartolino, Ellipsometry investigation of the effects of annealing temperature on the optical properties of indium tin oxide thin films studied by Drude–Lorentz model, *Appl. Surf. Sci.* 255/16 (2009) 7203-7211.
- [6] O. Medenbach, T. Siritanon, M. A. Subramanian, R. D. Shannon, R. X. Fischer, G. R. Rossman, Refractive index and optical dispersion of In_2O_3 , InBO_3 and gahnite, *Materials Research Bulletin*, 48/6 (2013) 2240-2243.
- [7] J. R. Bellingham, W. A. Phillips, and C. J. Adkins, *J. Phys.: Condens. Matter* 2 (1990) 6207-6221.
- [8] J. Kim, J. Bang, N. Nakamura and H. Hosono Ultra-wide bandgap amorphous oxide semiconductors for NBIS-free thin-film transistors, *APL Mater.* 7 (2019) 022501.
- [9] Y.-B. Lu, T. L. Yang, Z. C. Ling, W.-Y. Cong, P. Zhang, Y. H. Li and Y. Q. Xin, How does the multiple constituent affect the carrier generation and charge transport in multicomponent TCOs of In-Zn-Sn Oxide, *J. Mater. Chem. C*, 3 (2015) 7727-7737.
- [10] J.-W. Jeon, D.-W. Jeon, T. Sahoo, M. Kim, J.-H. Baek, J. L. Hoffman, N. S. Kim, I.-H. Lee Effect of annealing temperature on optical band-gap of amorphous indium zinc oxide film, *Journal of Alloys and Compounds* 509 (2011) 10062–10065.
- [11] C. Kranert, R. Schmidt-Grund, and M. Grundmann, Raman active phonon modes of cubic In_2O_3 , *physica status solidi (RRL)–Rapid Research Letters* 8/6 (2014) 554-559.
- [12] O. M. Berengue, A. D. Rodrigues, C. J. Dalmaschio, A. J. C. Lanfredi, E. R. Leite, and A. J. Chiquito, Structural characterization of indium oxide nanostructures: a Raman analysis, *Journal of Physics D: Applied Physics* 43/4 (2010) 045401.
- [13] D. Liu, W. Lei, S. Qin, L. Hou, Z. Liu, Q. Cui, and Y. Chen, Large-scale synthesis of hexagonal corundum-type In_2O_3 by ball milling with enhanced lithium storage capabilities, *J. Mat. Chem. A* 17/1 (2013) 5274-5278.
- [14] T. C. Damen, S. P. S. Porto, and B. Tell, Raman effect in zinc oxide, *Physical Review* 142/2 (1966) 570. <https://doi.org/10.1103/PhysRev.142.570>
- [15] D. N. Montenegro, V. Hortelano, O. Martínez, M. C. Martínez-Tomas, V. Sallet, V. Muñoz-Sanjosé, and J. Jiménez, Non-radiative recombination centres in catalyst-free ZnO nanorods grown by atmospheric-metal organic chemical vapour deposition, *Journal of Physics D: Applied Physics* 46/23 (2013) 235302.
- [16] J. S. Reparaz, L. R. Muniz, M. R. Wagner, A. R. Goñi, M. I. Alonso, A. Hoffmann, and B. K. Meyer, Reduction of the transverse effective charge of optical phonons in ZnO under pressure, *Appl. Phys. Lett.* 96 (2010) 231906.
- [17] J. García-Fernández, J. Bartolomé, A. Torres-Pardo, A. Peche-Herrero, J. Moreno, J. Ramirez-Castellanos, A. Cremades, J. M. González-Calbet, and J. Piqueras, Structural characterization at the atomic level and optical properties of the $\text{Zn}_k\text{In}_2\text{O}_{k+3}$ ($3 \leq k \leq 13$) system, *J. Mat. Chem. C* 5/39 (2017) 10176-10184.
- [18] J. S. Seo, J. H. Jeon, Y. H. Hwang, H. Park, M. Ryu, S. H. K. Park, and B. S. Bae, Solution-processed flexible fluorine-doped indium zinc oxide thin-film transistors fabricated on plastic film at low temperature, *Scientific reports* 3 (2013) 2085.
- [19] K. J. Chen, F. Y. Hung, and S. J. Chang, Structural characteristic, Raman analysis and optical properties of indium-doped ZnO nanoparticles prepared by sol–gel method, *Journal of nanoscience and nanotechnology* 9/5 (2009) 3325-3329.
- [20] Popov, V. N., Two-phonon Raman scattering in graphene for laser excitation beyond the π -plasmon energy, *Journal of Physics: Conference Series* 764 (2016) 012008
- [21] P. A. Temple, and C. E. Hathaway, Multiphonon Raman Spectrum of Silicon, *Phys. Rev. B* 7 (1973) 3685-3697.
- [22] M. V. Klein, Theory of two-phonon Raman scattering in transition metals and compounds, *Phys. Rev. B* 24/8 (1981) 4208-4223.